Modeling and Analysis of Neutrophil Transit through Individual Pulmonary Capillaries

by

Mark Bathe

B.S., Mechanical Engineering (1998)

Massachusetts Institute of Technology

Submitted to the Department of Mechanical Engineering
in Partial Fulfillment of the Requirements for the Degree of
Master of Science in Mechanical Engineering

at the

Massachusetts Institute of Technology

June 2001

BARKER

MASSACHUSETTS INSTITUTE OF TECHNOLOGY
JUL 16 2001
LIBRARIES

©2001 Massachusetts Institute of Technology
All rights reserved

Signature of Author.....
Department of Mechanical Engineering
April 17, 2001

Certified by.....
Roger D. Kamm
Professor of Mechanical Engineering
Thesis Advisor

Accepted by.....
Ain A. Sonin
Chairman, Department Committee on Graduate Students

MODELING AND ANALYSIS OF NEUTROPHIL TRANSIT THROUGH INDIVIDUAL PULMONARY CAPILLARIES

by

MARK BATHE

Submitted to the Department of Mechanical Engineering
on April 17, 2001 in partial fulfillment of the
requirements for the Degree of Master of Science in
Mechanical Engineering

ABSTRACT

The deformations characteristic of neutrophils as they pass through the microcirculation affect their transit time, their tendency to contact and interact with the endothelial surface, and potentially their degree of activation. In this study I investigate the effects of capillary entrance geometry and cell activation level on neutrophil transit through individual capillary segments in the pulmonary microvasculature. The neutrophil is modeled as a homogeneous viscoelastic Maxwell sphere bounded by constant surface tension and the capillary as a rigid, axisymmetric contraction of constant radius of curvature. Cell indentation experiments are simulated using the finite element method to determine appropriate Maxwell model constants (G_{cell} and μ_{cell}) for the cell in its passive and two levels of FMLP-activated states, corresponding to 1E-9 and 1E-6 M. The flow and deformation of the cells through individual capillary segments is subsequently analyzed using a fully coupled fluid-structure interaction finite element method. The indentation results indicate that neutrophil viscosity and shear modulus are strongly affected by the chemoattractant FMLP, increasing by factors of 3.4 (1E-9 M FMLP) and 7.3 (1E-6 M FMLP) over passive cell values, which were determined to be 30.8 Pa s and 185 Pa, respectively. Trans-capillary transit time is found to be approximately independent of cellular shear modulus provided that the shear modulus is more than about 20 times greater than the effective trans-capillary pressure drop. For this viscous deformation-dominated regime, the following simple expression, $T^* = 0.35\left(a^*\right)^{-0.58}\left[\left(R^*\right)^{-6.5} - 1\right]$, is derived to relate dimensionless cell transit time, $T^* = T\Delta p_{eff}/\mu_{cell}$, to dimensionless minimum constriction radius, $R^* = R_{min}/R_{cell}$, and dimensionless constriction radius of curvature, $a^* = a/R_{cell}$. The relative effects of FMLP and capillary geometry on neutrophil transit time in the pulmonary microcirculation are presented and their physiological implications discussed.

Thesis Supervisor: Roger D. Kamm

Title: Professor of Mechanical Engineering

Table of Contents

1. Introduction to Neutrophil Modeling and Simulation

1.1 Background

Leukocytes (white blood cells) are divided into three classes based on their structure and function, designated as granulocytes, monocytes, and lymphocytes. The neutrophil is one of three sub-types of granulocytes, the other two being basophils and eosinophils [1]. Neutrophils typically make up anywhere from 50% to 80% of the human white blood cell population and are important mediators of the inflammatory response.

Upon bacterial infection of the host, chemotactic signals are sent from the site of inflammation through the tissue and into the blood vessels to attract neutrophils. Upon arrival the neutrophil engulfs the bacteria and releases toxic oxides from its granules, thereby destroying both the harmful bacteria and the cell itself.

In order to be effective at fighting microbes in any part of the body, it is important that neutrophils be distributed throughout the body, both in the blood vessels and throughout the tissue. In addition, it is important that reservoirs of neutrophils exist in the body so that large quantities may be called upon at once to fight infection. These reservoirs are commonly referred to as "marginal pools" of cells and one of the most important ones exists in the lungs: the pulmonary microvasculature.

While it is well established that the lungs serve as a site of margination for neutrophils, it is not fully understood why the cells aggregate there. The working hypothesis that has been verified experimentally and via modeling to some degree [2, 3], is that neutrophils aggregate in the lungs due to their large average size (8 μm mean diameter) compared to the smaller pulmonary capillaries, which have an average diameter of 5.5 μm, and range in size from 2 to 15 μm, and due to their complex constitution (neutrophils have a multilobed nucleus in addition to a viscoelastic, actin-based cytoskeleton) compared to erythrocytes, which flow unhindered through the capillaries. In order to further test this hypothesis, however, it is critical that models be developed to better understand the effects of mechanical and biochemical factors on neutrophil transit time. Is neutrophil margination due to biochemical factors such as adhesion or cell activation level, mechanical factors, or some combination of both?

The essential role that the neutrophil plays in host defense in humans has led to strong interest in developing accurate mathematical models of these cells. With this aim, previous researchers have employed both experimental techniques [4, 5] and numerical methods [6, 7, 8] to understand, model, and predict the cell's response during micropipette aspiration as well as during its subsequent recovery.

While numerous researchers have concentrated their efforts on developing accurate neutrophil models applicable to micropipette aspiration experiments, few have attempted to use more realistic capillary geometries to understand *in vivo* neutrophil behavior, taking into account, for example, the effect of a gradually narrowing capillary geometry with variable constriction radius of curvature.

1.2 Objectives

The objectives of the present study are three-fold. The primary objective is to simulate the flow of a neutrophil through a mild pulmonary capillary constriction to quantify the effects of capillary geometry (both minimum constriction radius and

constriction radius of curvature) and cell activation level on cell transit time. The second objective is to model and simulate a cell indentation experiment to test the validity of several previously established neutrophil models under that experimental setting. The third goal is to use the indentation test to choose new cell model parameters that capture the passive and FMLP-activated response of the cell under indentation.

1.3 Approach

The three aforementioned objectives of this study are carried out as follows. First, three existing, well established continuum, passive neutrophil models are selected from the literature (Newtonian fluid with surface tension, Standard viscoelastic solid model, and Maxwell model with surface tension). The experimental basis for the individual models is presented, as well as their mathematical formulations and the published values of their parameters. The Maxwell model is used in the simulation of a micropipette aspiration experiment primarily for validation purposes. Subsequently, the three models are employed in cell indentation and their results compared to experiment. Due to the poor fit between the model results and experiment, the Maxwell model constants are then adjusted to best fit the experimental indentation data for a passive and two levels of FMLP-activated cells, because quantitative data are not available correlating FMLP-activation level with neutrophil viscosity and elastic stiffness. Finally, the capillary flow problem is simulated using two separate approaches. In the first, unsuccessful approach, the Newtonian cell model is employed using a fluid-fluid interface formulation that will be described in detail in the modeling sections to follow. The approach is unsuccessful because of its inability to solve the problem for physiological cell model parameter values. In the second, successful approach, the Maxwell cell model is employed using a fluid-structure interaction formulation. In this formulation contact is assumed to occur between the cell and capillary wall during transit, enabling the solution of the problem for the physiological Maxwell model parameter values determined in the indentation simulations. Verification of the analysis results is performed by comparing to analytical results when possible and to the simulation results of previous investigators when analytical results are unavailable.

Due to the nonlinear nature of the mathematical models employed in this study (fluid-structure interaction, changing boundary conditions, large displacements and deformations) and the complex geometries involved, a commercial finite element program (ADINA, Version 7.4) is used to solve the models.

2. The Neutrophil Models

Unlike erythrocytes, neutrophils are granulocytes and are thus complex in internal structure. They contain a multi-lobed nucleus that makes up about 20% of the cell's volume [9] in addition to a large number of cytoplasmic granules (Fig. 1a) that make up another 15%. The remainder of the cell consists primarily of cytoplasm. They are spherical in their undeformed state (Fig. 1b), with an outer diameter of between seven and 15 micrometers, and have both a cortex (indicated by the red dashed line in Figure 1a) and an outer lipid bilayer that contains a large excess of material (Fig. 1b). Despite their structural inhomogeneity, the cell interior (cytoplasm and nucleus) is traditionally modeled as a single, homogeneous medium. Only recently have any attempts been made at higher order, multi-component models that use separate domains for the cytoplasm and the stiffer nucleus [10, 11]. In all cases known to the author, traditional continuum mechanics is used to model the cell, neglecting the specific response of individual actin filaments in the cytoplasm, for example.

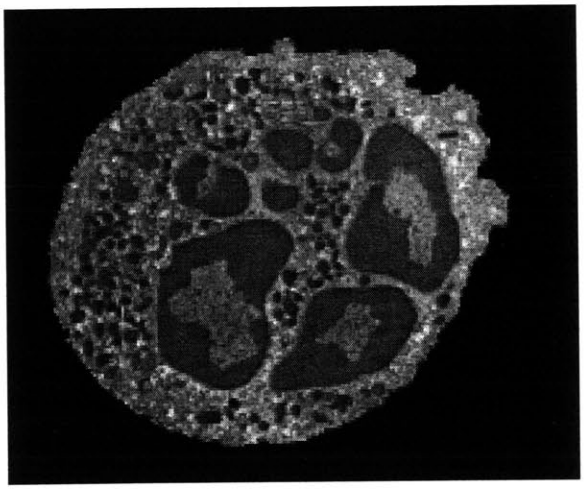

Fig. 1a A cross-sectional micrograph of a neutrophil illustrating the cell's multi-lobed nucleus, organelles, and numerous granules.

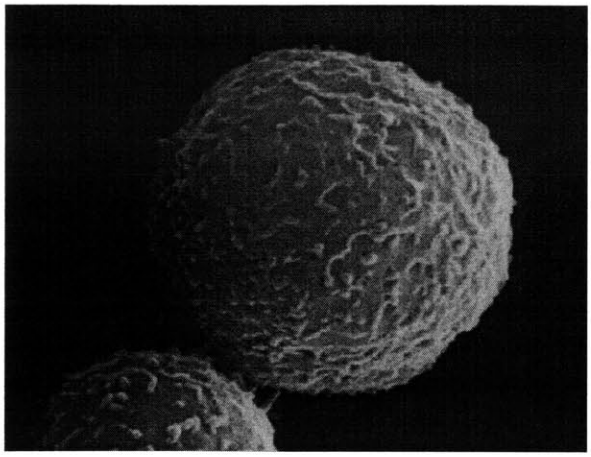

Fig. 1b Three-dimensional micrograph of a neutrophil in suspension illustrating its ruffled outer lipid bilayer and spherical undeformed configuration.

2.1 The Experimental Basis for the Models

There are a number of critical experimental observations [12] that have been used to establish the primary (or first order) model components of a neutrophil. All of the observations have been made in micropipette aspiration experiments where the cell is aspirated from a suspending medium into a smaller diameter pipette using a step pressure loading of varying magnitude. Figure 2 shows results typical of a micropipette aspiration experiment.

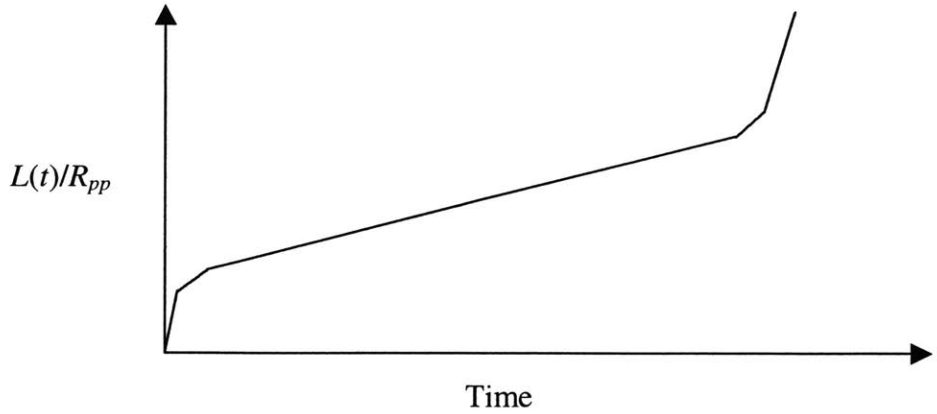

Fig. 2 Typical experimental results of neutrophil aspiration into a micropipette under a constant driving pressure difference. R_p is the inner radius of the pipette and $L(t)$ is the protrusion of the cell tip into the pipette.

The primary findings of the micropipette aspiration experiment are:

1. The cell undergoes an (almost) instantaneous deformation a short distance into the pipette.
2. There exists a critical pressure drop, Δp_{crit}, above which the cell continuously flows into the pipette. Furthermore, this critical pressure drop corresponds to a cell configuration in which the portion of the cell that is inside the pipette has forms a hemisphere with diameter equal to the inside diameter of the pipette.
3. If after flowing for some time, the pressure drop is reduced to Δp_{crit}, the cell recoils slightly but remains extended in the pipette.
4. During the period of continuous, liquid-like flow, the portion of the cell that is outside of the pipette remains approximately spherical.
5. After the initial elastic response, the rate of entry of the cell scales approximately linearly with the applied pressure drop.
6. The total volume of the cell is preserved during aspiration.
7. There exists a limit to the increase in surface area of the cell of about 100% that is imposed by the lipid bilayer. Beyond this increase in cell surface area lysis of the lipid bilayer occurs.

The corresponding mathematical model parameters/characteristics are:

1. & 3. The cell exhibits a small degree of elasticity that is characteristic of the response of an elastic solid.

2., 3., and 4. The cell behaves as though it were bounded by a small, constant, surface tension-like force. An actin-rich layer at the lipid bilayer membrane surface probably causes this "cortical tension".

2., 3., and 5. The bulk of the response time of the cell is characteristic of that of a highly viscous, linear Newtonian fluid.

6. The cell is incompressible.
7. The cell surface area may not increase beyond 100%.

The critical pressure drop above which a viscous droplet bounded by a constant surface tension continuously flows into a pipette is given by the following relationship

$$\Delta p_{crit} = 2\gamma\left(\frac{1}{R_p} - \frac{1}{R_{cell}}\right) \tag{2.1}$$

where γ is the constant coefficient of surface tension, R_p is the inner radius of the pipette, and R_{cell} is the undeformed droplet (cell) radius, which is used to approximate the radius of curvature of the cell surface that is outside the pipette. It is important to note in Eqn. (2.1) that the radius of curvature of the droplet (or cell) external to the pipette is approximated to be equal to the undeformed droplet radius, and that this approximation becomes worse as larger pipette sizes are considered, or geometries such as tapered constrictions are considered (where the critical pressure is assumed to be the maximum critical pressure, which occurs when the cell reaches the minimum constriction point).

2.2 The Models

The three more popular or "well-founded" neutrophil models are

1. Standard viscoelastic solid
2. Maxwell material with surface tension
3. Newtonian fluid with surface tension

Although each model has its individual strong and weak points (to be discussed later), each one has been founded on experimental observations of either micropipette aspiration or cell recovery after full aspiration or both. For this reason it is not unreasonable to expect that the models will not perform well when tested under very different loading conditions, such as in cell indentation. The first two incorporate the observed initial elastic response of the cell to the step pressure, whereas the last one does not. All three incorporate the flowing behavior of the cell that is characteristic of a viscous fluid, although the first does not incorporate the surface tension effect of the cortex and has a static limit to deformation (when Δp_{crit} is exceeded) whereas the other two do not (they continuously flow). Additionally, all three neglect bending stiffness in the cortex. Cortical bending stiffness has been shown to be negligible for all but the very smallest radii of curvature, as would be encountered in cell aspiration into pipettes of diameter less than two micrometers [13].

2.2.1 Standard Viscoelastic Solid Cell Model

This model is one of the earliest continuum neutrophil models and was pioneered by Schmid-Schönbein et al. in 1981 [5]. In this model the cell is assumed to be a homogeneous, incompressible sphere *without* cortical tension, with its deviatoric response modeled by a standard viscoelastic solid element, in which an elastic spring is in parallel with a spring-dashpot series element. The governing constitutive equations for the bulk and deviatoric responses are [14], respectively,

$$p = -\kappa E_v \tag{2.2}$$

$$\dot{\mathbf{T}}' + \frac{k_2}{\eta_2}\mathbf{T}' = (k_1 + k_2)\dot{\mathbf{E}}' + \frac{k_1 k_2}{\eta_2}\mathbf{E}' \tag{2.3}$$

or, using the following definitions of k_i and η

$$k_1 = 2G_1$$
$$k_2 = 2G_2$$
$$\eta_2 = 2\mu_2$$

the deviatoric response can be written as

$$\dot{\mathbf{T}}' + \frac{G_2}{\mu_2}\mathbf{T}' = 2(G_1 + G_2)\dot{\mathbf{E}}' + \frac{2G_1 G_2}{\mu_2}\mathbf{E}' \tag{2.4}$$

where $\mathbf{T}'$ and $\mathbf{E}'$ are the deviatoric Cauchy stress and small strain tensors, respectively, defined in Appendix A, p and E_v are the mechanical pressure and the volumetric strain, respectively, also defined in Appendix A, k_1 is twice the elastic shear modulus ($2G_1$) for the first spring element, k_2 is twice the elastic shear modulus (G_2) for the second spring element, η_2 is the viscosity of the dissipative Maxwell element and equal to twice the equivalent Newtonian fluid viscosity ($2\mu_2$), κ is the bulk modulus (and $\kappa \to \infty$ for an incompressible medium), and a superimposed dot denotes time differentiation.

For short time scales, or infinitely fast deformation, (deformation time scales that are much shorter than τ_n defined in Eqn. (2.5) below) the standard viscoelastic solid responds in shear like a linear elastic solid with shear modulus $\left(\frac{k_1 + k_2}{2}\right)$, or simply ($G_1$ + G_2). For long time scales or infinitely slow deformation, it responds as a linearly elastic solid with shear modulus $\frac{k_1}{2}$ or G_1. The time constant associated with the relaxation of stress in the solid is given by

$$\tau_n = \frac{\eta_2}{k_2} = \frac{2\mu_2}{2G_2}. \tag{2.5}$$

2.2.2 Maxwell Model with Cortical Tension

Dong *et al.* pioneered this model in 1988 [15]. In this model the cell is also treated as homogeneous and incompressible. The difference with the standard solid model is that here the deviatoric response is modeled using the Maxwell element, in which there is only an elastic element in series with a dashpot, and the cortical tension is explicitly accounted for with constant surface tension. The governing constitutive equations for the bulk and deviatoric responses are [14], respectively,

$$p = -\kappa E_v \tag{2.6}$$

$$\dot{\mathbf{E}}' = \frac{\dot{\mathbf{T}}'}{k_2} + \frac{\mathbf{T}'}{\eta_2} \tag{2.7}$$

where again, using the following definitions

$$k_2 = 2G_2$$
$$\eta_2 = 2\mu_2$$

we have for the deviatoric response

$$\dot{\mathbf{E}}' = \frac{\dot{\mathbf{T}}'}{2G_2} + \frac{\mathbf{T}'}{2\mu_2} \tag{2.8}$$

where all the notation has been previously defined.

Referring to the constitutive form of Eqn. (2.8), it is clear that if G_2 is infinite and μ_2 finite, then there is zero instantaneous elastic response to an applied stress, and the Maxwell model reduces to that of a linear Newtonian fluid with viscosity μ_2. Alternatively, if μ_2 is infinite and G_2 finite, then there is zero deviatoric strain rate associated with a constant applied stress and the material behaves like an elastic solid governed by Hooke's law. (Glass is an example of a Maxwell type of material that is commonly treated simply as an elastic material because it only flows over very long time scales (centuries).)

For very short time scales ($t << \tau_n$), a Maxwell material responds in pure shear like an elastic solid with a shear modulus of k_2 (G_2), whereas for longer time scales ($t >> \tau_n$) the material flows like a fluid with viscosity η_2 ($= \mu_2$). The time scale of stress relaxation is the same as in the standard solid model above.

The cortical tension is accounted for explicitly in this model by assuming that a surface tension force exists on the outer periphery of the cell (the cortex). This surface tension force can be expressed for a cell with no externally applied tractions as

$$\mathbf{n} \cdot \mathbf{T}\mathbf{n} = 2H\hat{\gamma} \quad \text{on } S \tag{2.9}$$

where S is used to denote the bounding surface of the cell, $\mathbf{n}$ is the outward unit normal to the cell surface, $\mathbf{T}$ is the total Cauchy stress tensor, $\hat{\gamma}$ is the constant coefficient of surface tension, and H is the mean curvature of the bounding surface and assumed positive when the center of curvature lies in the direction of the surface normal.

The mean curvature of a surface, H, is found by taking any two orthogonal planes that contain the normal of the surface at the point of interest (the intersection of the two planes is coincident with the normal) and averaging the inverses of the radii of curvature of the two curves formed by the intersection of the orthogonal planes with the surface

$$H = \frac{1}{2}\left(\frac{1}{R_1} + \frac{1}{R_2}\right). \tag{2.10}$$

2.2.3 Newtonian Fluid Model with Cortical Tension

Evans & Yeung pioneered this model in 1989 [8]. In this model the cell is modeled as a simple, linear Newtonian fluid with constant surface tension (essentially a highly viscous liquid droplet with surface tension). The governing constitutive equation is

$$\mathbf{T} = -p\mathbf{I} + 2\mu\mathbf{D} \tag{2.11}$$

where p is the fluid pressure (mechanical or thermodynamic, they are equal for an incompressible fluid), μ is the coefficient of laminar viscosity, and $\mathbf{D}$ is the rate of strain tensor defined by

$$\mathbf{D} = \frac{1}{2}\left(\mathbf{L} + \mathbf{L}^{T}\right)$$
$$\mathbf{L} = \text{grad}\,\mathbf{v} \tag{2.12}$$

where $\mathbf{v}$ is the material (fluid) velocity and the gradient operator is with respect to the current configuration (spatial coordinates). Clearly this model does not contain any elastic response and therefore entirely neglects the cell's inherent elasticity. The spherical shape of the cell is nonetheless its equilibrium configuration (in the absence of external tractions or body forces) due to the cortical tension in the model. The cortical tension in this model is mathematically equivalent to that of the Maxwell model described in Section 2.2.2 (see Eqns. (2.9) and (2.10)).

3 Governing Equations

3.1 Geometry

Micropipette Aspiration

The initial configurations of the rigid, axisymmetric pipette and undeformed spherical cell are shown in Figure 3. The radius of the cell is R_{cell}, the inner radius of the pipette, $R_{pipette}$, and the thickness of the pipette is denoted by h. The radius of curvature of the pipette tip is simply $h/2$. In the results section, $d(t)$ is used to denote the displacement of the cell from its initial position shown in Figure 3. Numerical values of the geometric parameters used in the analysis are consistent with the simulation performed by Dong *et al.* [15] and are listed in Table I.

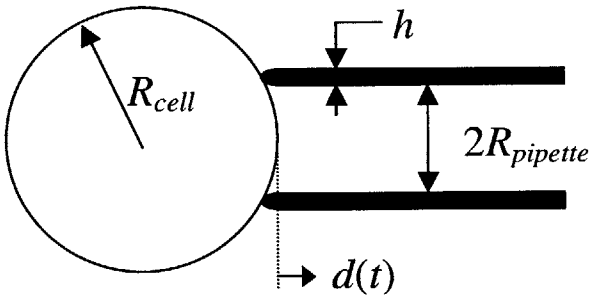

Fig. 3 Original configuration of cell and pipette used for small deformation pipette simulation (pipette is assumed to be a rigid contact surface).

Table I Pipette and undeformed cell dimensions for small deformation cell aspiration simulation (after Dong et al. [15]).

R_{cell}	4.27 μm
$R_{pipette}$	2.14 μm
h	0.43 μm

Indentation

The initial configuration of the axisymmetric indenter, undeformed cell, and rigid substrate are shown in Figure 4. The radius of the cell is R_{cell}, the maximum radial dimension of the indenter is $R_{indenter}$, the radius of curvature of the indenter corners is $\rho_{indenter}$, and the length of the indenter is $L_{indenter}$. During indentation the geometry of the cell evolves due to the deformation imposed by the action of the indenter and support of the substrate. Numerical values of geometric and other model parameters, such as indentation rate and maximum indentation depth are tabulated in Table II and consistent with the simplified analytical models presented by Zahalak *et al.* [16].

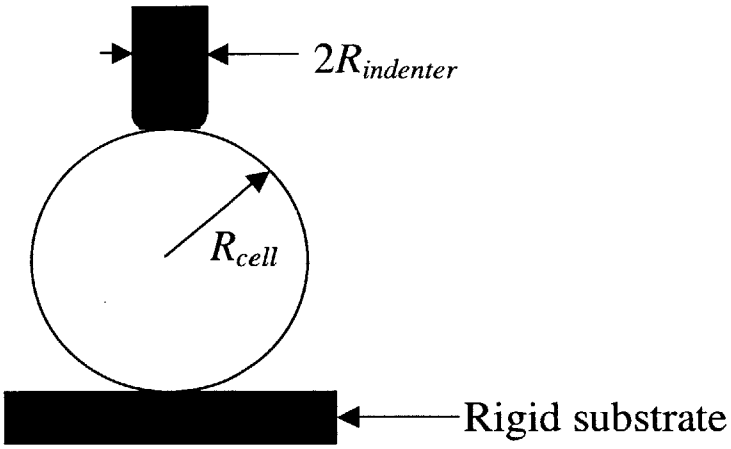

Fig. 4 Original configuration of cell and indenter used for indentation simulations (indenter and substrate are assumed to be rigid).

Table II Indentation simulation parameters (adopted from Zahalak *et al.* (1990)).

$\rho_{indenter}$	R_{cell}	$R_{indenter}$	Maximum Indentation	Indentation Rate
0.15 μm	4 μm	1 μm	1.5 μm	5.1 $\mu m/s$

Capillary Flow

Figure 5 shows the idealized axisymmetric capillary geometry and contact surface used for the fluid-structure interaction capillary flow simulations, as well as the assumed initial position and configuration of the cell. As usual, the cell was assumed to be spherical in its initial, undeformed configuration, with radius R_{cell}. The capillary was assumed to be cylindrical upstream and downstream of the constriction, with radius $R_{capillary}$. The constriction varies smoothly from inlet to outlet and is described in cross-section by an arc of constant radius of curvature. The radius of curvature of the contact surface is denoted a, and the radius of curvature of the capillary wall is given by the quantity $(a-\delta)$, where δ is the constant gap thickness between the capillary wall and the contact surface. The gap thickness, δ, was chosen to be constant and equal to 100 nm, treating the glycocalyx as a rigid layer that is highly permeable to the flow of plasma, and was a compromise between a more complex model, such as that employed by Feng and Weinbaum, (2000) and having no layer, in which case the cell would be allowed to approach within 10 nm of the capillary wall. Choosing the right-handed cylindrical coordinate system (r, θ, z) shown in Figure 5, where the origin of the system has been chosen to coincide with the intersection of the capillary axis and the plane that is normal to that axis and contains the midpoint of the constriction, the contact surface constriction radius, $R(z)$, can be expressed analytically as

$$R(z)=(R_{min}+a)-\sqrt{a^2-z^2} \quad \text{for} \quad (-l\le z\le l) \tag{3.1}$$

where z denotes position along the capillary axis, R_{min} is the minimum constriction radius, and $2l$ is the total axial length of the constriction.

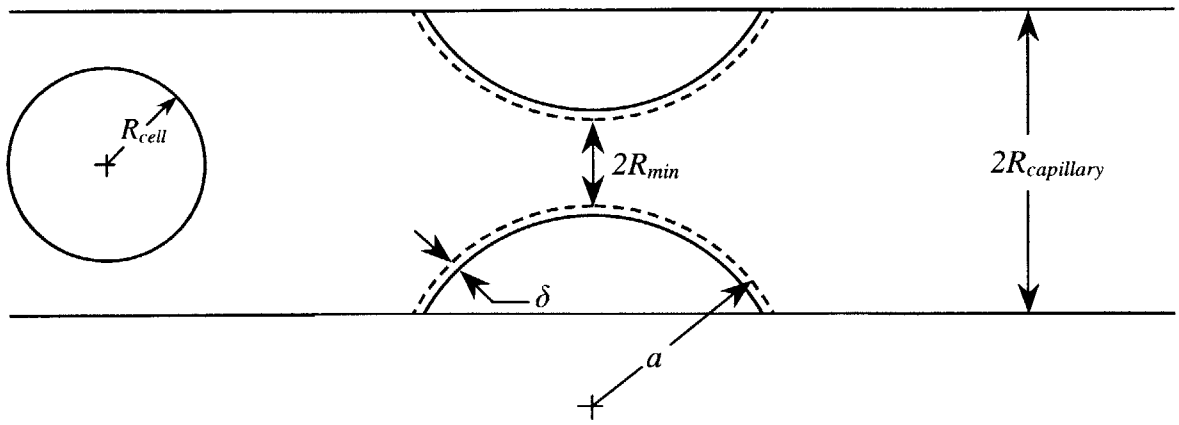

Fig. 5 Geometry for fluid-structure interaction neutrophil-capillary flow model.

3.2 Equations of Motion and Mass Conservation

Solving a boundary value problem involving any of the above neutrophil models requires a set of partial differential equations (in addition to the constitutive laws) provided by momentum, continuity, and boundary/initial conditions. In its most general form, the momentum equation can be written for solids and fluids as

$$\rho \dot{\mathbf{v}} = \operatorname{div} \mathbf{T} + \mathbf{b} \tag{3.2}$$

where the time derivative in Eqn. (3.2) is a material time derivative (i.e. following a material particle), ρ is the (constant) material density, $\mathbf{b}$ denotes a generic body force such as gravity, and all other symbols have previously been defined.

Despite the fact that the applications of the methods presented here do not require the inertia or the body force term in Eqn. (3.2), the terms will be retained for greater generality of the formulations.

Incompressibility for the plasma and for the Newtonian fluid cell model, which is formulated using the Arbitrary Lagrangian Eulerian formulation, requires that the velocity fields be divergence free in the plasma and cell domains, and can be written as

$$\operatorname{div} \mathbf{v} = 0. \tag{3.3}$$

(Mass conservation is automatically satisfied for the viscoelastic cell models because they are formulated using Lagrangian formulations.)

3.3 Constitutive Equations

The specific constitutive equations depend upon the particular cell model employed. In both viscoelastic models, near incompressibility is assumed ($\nu = 0.499$) due to the inability of ADINA to model exactly incompressible viscoelastic media ($\nu = 0.5$), so that $\kappa = 500G$. Furthermore, the shear modulus, G is given in each case by the model constants k_1, k_2, and η_2 determined by previous investigators (Table III) or from previous indentation experiments, in this study (Table IV). Viscoelastic material data is input into ADINA using Prony or Dirichlet Series, given in Eqns. (3.6) and (3.7) below for the standard solid and Maxwell model shear moduli, repectively, and by Eqn. (3.16) for the bulk moduli.

An alternative, integral representation of the differential viscoelastic constitutive equations given in Section 2.2 can be derived as follows. Consider a creep test, in which a step constant stress is applied to the material, and the resulting strain measured as a function of time. We then have that

$$\gamma(t) = \tau_0 J(t) \tag{3.4}$$

where τ_0 is the constant, step stress applied to the material, $\gamma(t)$ is the time-dependent (in general) strain resulting from the applied stress, and $J(t)$ is defined to be the *creep compliance*, relating the two (note that the creep compliance is a function which can be measured experimentally for any given material, and in general is different for different types of viscoelastic materials). Similarly, we can apply a constant strain, γ_0, to the material and measure the stress as a function of time

$$\tau(t) = \gamma_0 G(t) \tag{3.5}$$

where $G(t)$ is called the *relaxation modulus*, and is also different for different types of materials. For the case of the standard viscoelastic solid model, the relaxation modulus is

$$G(t) = G_\infty + G_2 e^{-\frac{t}{\tau_n}} \tag{3.6}$$

where G_∞ is termed the *environmental* shear modulus, representing the effect of the parallel spring that provides a static limit to deformation (or a finite, non-decaying stress for any applied strain), G_2 represents the Maxwell, series spring, which dissipates its stored elastic energy through the series dashpot, and τ_n is the characteristic Maxwell time constant or decay time, which is equal to μ_2/G_2 or η_2/k_2. The decay time, τ_n, corresponds to the time that the stress resulting from a constant step applied strain would relax to zero if it were to relax at its initial rate of relaxation (in fact the rate of relaxation is a decaying function of time). For a simple Maxwell material, the relaxation modulus is given as

$$G(t) = Ge^{-\frac{t}{\tau_n}}. \tag{3.7}$$

Next, we note that we may express an arbitrary constant stress, τ_1, that is applied to the material at time $t = \xi_1$, as a function of time $\tau(t) = \tau_1 H(t - \xi_1)$, where $H(t)$ is the Heaviside function, equal to zero for times less than t, ½ at time t, and 1 for times greater than t. Using (3.4), we can then express the time-dependent strain resulting from this constant stress as

$$\gamma(t) = \tau_1 J(t) H(t - \xi_1). \tag{3.8}$$

We now generalize this concept by considering a series of n incremental constant stresses applied to the material at various points in time, ξ_i. The total stress applied to the material as a function of time is then simply a linear superposition of the stress increments $\Delta\tau_i$,

$$\tau(t) = \sum_{i=1}^{n} \Delta\tau_i H(t - \xi_i). \tag{3.9}$$

Since we are only considering linear viscoelastic materials, in which strain is linearly related to stress, we may superimpose the separate strains resulting from separate stress increments to obtain the total strain resulting from the sum of the stresses,

$$\gamma(t) = \sum_{i=1}^{n} \gamma_i(t - \xi_i) = \sum_{i=1}^{n} \Delta\tau_i J(t - \xi_i) H(t - \zeta_i). \tag{3.10}$$

If we now consider the continuous limit of Eqn. (3.10), in which we apply infinitely many small increments in stress throughout time so that the total stress as a function of time is a smoothly varying, differentiable function, we have

$$\gamma(t) = \int_0^t J(t - \xi) H(t - \xi) d\tau(\xi). \tag{3.11}$$

Since the Heaviside function in Eqn. (3.11) is always equal to one because t is always greater than ξ, we can re-write the equation as

$$\gamma(t) = \int_0^t J(t - \xi) \frac{\partial \tau(\xi)}{\partial \xi} d\xi. \tag{3.12}$$

Employing the exact same arguments for the relaxation test, we can similarly derive the following expression for the time-dependent stress resulting from an arbitrary time-dependent strain as

$$\tau(t) = \int_0^t G(t - \xi) \frac{\partial \gamma(\xi)}{\partial \xi} d\xi. \tag{3.13}$$

Eqn. (3.13) can be generalized to three dimensions in a straightforward manner using the definitions of deviatoric stress, $\mathbf{T}'$, and deviatoric strain, $\mathbf{E}'$, introduced earlier as

$$\mathbf{T}'(t)=\int_0^t 2G(t-\xi)\frac{\partial \mathbf{E}'(\xi)}{\partial \xi}d\xi \tag{3.14}$$

and similarly for the bulk response we have

$$T_{kk}(t)=\int_0^t 3\kappa(t-\xi)\frac{\partial E_{kk}(\xi)}{\partial \xi}d\xi \tag{3.15}$$

where $G(t)$ is the shear relaxation modulus given above for the Maxwell and standard solid models and $\kappa(t)$ is the hydrostatic (or bulk) stress relaxation modulus, related to the shear relaxation modulus by

$$\kappa(t)=\frac{2(1+\nu)}{3(1-2\nu)}G(t). \tag{3.16}$$

Table III: Various published neutrophil model properties.

Model	k_1 (Pa)	k_2 (Pa)	η_2 (Pa s)	$\hat{\gamma}$ (pN/μm)	τ_n (s)	Reference
Standard Viscoelastic Solid	27.5	73.7	13.0	0	0.176	(5)
Maxwell with surface tension	0	28.5	30.0	31	1.05	(15)
Newtonian with surface tension	0	0	210	35	∞	(8, 12)

3.4 Boundary and Initial Conditions

In addition to the surface tension boundary conditions on the Maxwell and Newtonian cell models, there are boundary conditions that are specific to the particular problem of interest, i.e. pipette aspiration, cell indentation, or capillary flow.

Pipette Aspiration

In the pipette aspiration simulations a negative pressure is prescribed at the cell surface interior to the pipette and zero pressure exterior to the pipette. This pressure loading models the applied pressure drop in the experiments with which we compare the model results. The reason it is applied negatively from the interior of the pipette vs. positively from the exterior is to avoid elastic buckling in the viscoelastic cell models.

Note that due to incompressibility, the nature of the solution is not changed by this modeling assumption, however the buckling is avoided. In the cases of the models with surface tension, the stress boundary condition (Eqn. (2.9)) on the cell surface inside the pipette becomes

$$\mathbf{n}\cdot\mathbf{Tn} = 2H\hat{\gamma} - \Delta p \quad \text{on } S_{inside} \tag{3.17}$$

where Δp is the experimentally applied pressure drop (assumed positive), whereas the boundary condition on the cell surface exterior to the pipette remains only that due to the surface tension force (Eqn. (2.9)). Both boundary conditions are nonlinear due to the fact that the cell surface evolves in time in the analysis.

In addition to these boundary conditions there is an additional natural, nonlinear boundary condition that is due to the pipette. The contact boundary condition available in ADINA was used to ensure that the cell surface slides along the pipette tip and interior as it is aspirated, with zero friction. A distributed normal force is applied to the cell surface by this algorithm to ensure that this boundary condition is met (for more information on the details of the contact algorithm used in ADINA see ref. 16).

Cell indentation

In the cell indentation simulations frictionless contact conditions were assumed between the indenter and cell, and between the cell and substrate. A constant velocity was applied to the top center of the indenter and reversed when the indenter reached its maximum indentation depth of 1.5 μm (achieved in 0.29 seconds, refer to Table II).

Capillary Flow

In the capillary flow simulations each of the neutrophil models was suspended in plasma that was modeled as an incompressible Newtonian fluid with the viscosity and density of water. The mixed boundary conditions on the plasma and the interfacial conditions on the cell-plasma interface are described below.

As previously mentioned, two separate capillary flow models were tested and employed in this study. In the first, a fluid-fluid interface analysis procedure was employed, using an Arbitrary Lagrangian Eulerian (ALE) formulation for both the cell and plasma. Due to the fluid formulation used for the cell, only the Newtonian cell model could be employed using this procedure. In the second capillary flow model, a fluid-structure interaction analysis procedure was employed, using a solid (Lagrangian) formulation for the cell and a fluid (ALE) formulation for the plasma. For this model, the viscoelastic Maxwell model was employed. In both the fluid-fluid interface model and the fluid-structure interaction model the following interfacial and boundary conditions were satisfied, although the kinematic formulations and numerical approaches to solving the equations of motion differed considerably and will be described in Section 4.

Fluid-fluid Interface Model

Plasma

The natural boundary conditions imposed on the plasma at the inlet and outlet of the capillary were

$\mathbf{Tn}\cdot\mathbf{n} = 0$ at the capillary inlet (upstream of the constriction)

$\mathbf{Tn} \cdot \mathbf{n} = -\Delta p$ at the capillary outlet (downstream of the capillary constriction)

And the essential boundary condition imposed on the capillary walls was

$\mathbf{v} = \mathbf{0}$ on the capillary walls (no slip).

Cell-Plasma Interfacial Conditions

The cell-plasma interfacial conditions were continuity of velocity and shear stress, and discontinuity of normal stress due to the surface tension. The velocity condition can be expressed as

Velocity Continuity (or no slip)

$$\mathbf{v}^{cell} = \mathbf{v}^{plasma} \quad \forall t \tag{3.18}$$

and the interfacial normal stress jump has been previously given in Eqn. (2.9).

Fluid-structure Interaction Model

Plasma

The boundary conditions on the plasma are identical to those in the previous section above.

Cell-Plasma Interfacial Conditions

The interfacial conditions between the cell and plasma are also identical to those in the previous section.

Cell-Capillary Wall Contact Condition

The primary difference between the fluid-fluid interface model and this one is that contact was assumed to occur between the cell and capillary wall when the gap thickness between the cell and wall reached 0.1 μm. This assumption is what allowed the model to be solved for the physiologically realistic cell viscosities and shear moduli determined via cell indentation in Section 5.2. When in contact, nonlinearly varying natural boundary conditions were applied to the cell in order to ensure that the contact surface was not penetrated. Contact between the contact surface and cell was assumed to be frictionless, so that only a normal traction was applied to the cell by the contact surface. Both normal and shear components of the fluid (plasma) traction were applied to the cell throughout the analysis, however, regardless of whether the cell was in contact or not. For details on the contact algorithm employed in ADINA, the reader is referred to Reference 17 (Bathe, KJ) and the ADINA User Manuals [18].

4. Finite Element Methods

As mentioned earlier in Section 1, all of the problems of interest in this study are nonlinear and therefore require numerical methods for their solution. The numerical method that has been chosen in this study due to its flexibility in modeling complicated geometries, large deformations, multi-physics problems (coupled fluid-structure interaction), and nonlinear contact problems is the finite element method.

In this section, the general approach of the finite element solution of continuum mechanics solid and fluids problems will be addressed.

4.1 Discretization of the Governing Equations

4.1.1 The Principle of Virtual Work

The Principle of Virtual Work is the fundamental theorem upon which the finite element method is based, and is used in developing the discretized form of the governing fluid and solid equations. The only difference between the two derivations is that the principle is written on a rate (power) basis for the fluid equations vs. a work (energy) basis for the solid equations. This is due to the fact that in solving fluids problems an Eulerian formulation is typically employed in which material velocity is used as an independent variable vs. solids problems, where a Lagrangian formulation is typically employed in which material displacement is used as an independent variable.

The Solid Equations

The principle of virtual work is derived from the following "virtual" mechanical energy statement,

$$\int_{Vol} \rho \mathbf{b} \cdot \delta \bar{\mathbf{u}} \, dV + \int_{S} \mathbf{t}_{(\hat{\mathbf{n}})} \cdot \delta \bar{\mathbf{u}} \, dS = \text{Increment in Virtual Work} \tag{4.1}$$

where $\delta \bar{\mathbf{u}}$ is an imaginary (virtual) increment in displacement of the material particles in the body, the volume integral accounts for the virtual work done onto the body by externally applied body forces **b**, and the surface integral accounts for virtual work done on the body by externally applied tractions, $\mathbf{t}_{(\mathbf{n})}$. Clearly this external "virtual" work must either go into increasing the stored elastic energy in the body, increasing the kinetic energy of the body, or be dissipated in the body by viscous effects. Using the fact that

$$\mathbf{t}_{(\hat{\mathbf{n}})} = \mathbf{T}\hat{\mathbf{n}}, \tag{4.2}$$

and the divergence theorem, Eqn. (4.1) may be recast into the following, equivalent form (see Appendix B)

$$\int_{Vol} \rho \mathbf{b} \cdot \delta \bar{\mathbf{u}} \, dV + \int_{S} \mathbf{t}_{(\mathbf{n})} \cdot \delta \bar{\mathbf{u}} \, dS = \int_{Vol} (\rho \mathbf{b} + \operatorname{div} \mathbf{T}^{T}) \cdot \delta \bar{\mathbf{u}} \, dV + \int_{Vol} \mathbf{T} \cdot \delta \bar{\mathbf{E}} \, dV. \tag{4.3}$$

The momentum equation (Eqn. (3.2)) may then be used to reduce Eqn. (4.3) to its final form

$$\int_{Vol} \mathbf{T} \cdot \delta \bar{\mathbf{E}} \, dV = \int_{Vol} \rho(\mathbf{b} - \dot{\mathbf{v}}) \cdot \delta \bar{\mathbf{u}} \, dV + \int_{S} \mathbf{t}_{(\mathbf{n})} \cdot \delta \bar{\mathbf{u}} \, dS \tag{4.4}$$

where the body force and divergence terms on the right hand side of Eqn. (4.3) have been substituted for with the inertial term in the momentum equation.

Eqn. (4.4) is the fundamental form of The Principle of Virtual Work. It expresses the fact that if an arbitrary set of virtual displacements are imposed onto a body at any instant in time during the motion of the body, then the virtual work done by the external body forces and tractions onto the body contributes to 1. an increase in the velocity of the material particles in the body (increased kinetic energy) and 2. the pure deformation of fibers in the body, resulting in an elastic storage of the virtual work increment in the body, a viscous dissipation of the work, or a combination of the two. Eqn. (4.4) is a statement of mechanical energy conservation and holds irrespective of the type of material the body is composed of.

Eqn. (4.4) is used in developing the discretized form of the governing solid equations because it has been written using displacements as the primary unknown variables, and hence lends itself to a Lagrangian description vs. an Eulerian description which would employ velocities as primary unknowns and will be turned to next.

The Fluid Equations

The governing fluid equations are discretized in the same manner as the solid equations. The only difference is that the primary unknowns are velocities, so that The Principle of Virtual Work is written on a rate basis (Principle of Virtual Power) rather than an energy basis:

$$\int_{Vol} \mathbf{T} \cdot \bar{\mathbf{D}} \, dV = \int_{Vol} \rho(\mathbf{b} - \dot{\mathbf{v}}) \cdot \bar{\mathbf{v}} \, dV + \int_{S} \mathbf{t}_{(\mathbf{n})} \cdot \bar{\mathbf{v}} \, dS \tag{4.5}$$

where all quantities have previously been defined.

4.1.2 Discretized Form of the Governing Equations

Going from the Principle of Virtual Work statement (Eqn. (4.4)) to the discretized form of the governing equations in the finite element method requires the use of interpolation functions for the primary unknowns (displacements/velocities). Using standard notation for the interpolation functions we have for the displacements and the strains in a typical 2D element

$$\mathbf{u}(x, y) = \mathbf{H}\hat{\mathbf{u}} \tag{4.6}$$

$$\mathbf{E}(x, y) = \mathbf{B}\hat{\mathbf{u}} \tag{4.7}$$

where $\hat{\mathbf{u}}$ denotes the nodal displacement degrees of freedom for a typical finite element. Upon substitution into the left-hand side of Eqn. (4.4) we have

$$\mathbf{F} = \int_{Vol} \mathbf{B}^{\mathrm{T}}\mathbf{T}\,\mathrm{dV} \tag{4.8}$$

where **F** is used to denote the vector of forces onto the finite element nodes due to the internal stresses in the body. Furthermore, upon substitution into the terms on the right hand side of Eqn. (4.4) we have the following forcing terms

$$\mathbf{R}_t = \int_S \mathbf{H}^{\mathrm{T}}\mathbf{t}_{(\mathbf{n})}\,\mathrm{dS} \tag{4.9}$$

$$\mathbf{R}_b = \int_{Vol} \mathbf{H}^{\mathrm{T}}\left(\mathbf{b} - \dot{\mathbf{v}}\right)\mathrm{dV} \tag{4.10}$$

where $\mathbf{R}_S$ denotes the vector of forces onto the finite element nodes due to external tractions and $\mathbf{R}_b$ is used to denote the vector of forces onto the finite element nodes due to external body forces. The extension of these equations from a single element to an assemblage of finite elements simply requires a summation over all elements in the finite element model.

Thus the continuous form of the Principle of Virtual Work reduces to the following statement of equilibrium in discretized form

$$\mathbf{F} = \mathbf{R}_t + \mathbf{R}_b\,. \tag{4.11}$$

Eqn. (4.11) is what we *want* to satisfy such that at every time step in our analysis we satisfy equilibrium, and next we address *how* that equilibrium is reached through iteration on the finite element equations.

4.1.3 Solution of Equations and Newton Raphson Iteration

Eqn. (4.11) can be written in simplified form as

$$\mathbf{0} = \mathbf{R}(\mathbf{u}) - \mathbf{F}(\mathbf{u}) \tag{4.12}$$

or simply

$$\mathbf{f}(\mathbf{u}) = \mathbf{0} \tag{4.13}$$

where now **R(u)** is used to denote the sum of the body forces and all external tractions and their (nonlinear) dependence on the nodal degrees of freedom, **u**. In order to obtain the solution, **u**, to Eqn. (4.13) numerically we first expand **f(u)** using a Taylor series expansion

$$\mathbf{f}(\mathbf{u} + \Delta\mathbf{u}) = \mathbf{f}(\mathbf{u}) + \frac{\partial \mathbf{f}(\mathbf{u})}{\partial \mathbf{u}}\Delta\mathbf{u} + H.O.T. \tag{4.14}$$

and set the right hand side equal to zero since our goal is to reach $\mathbf{f}(\mathbf{u} + \Delta\mathbf{u}) = \mathbf{0}$:

$$\mathbf{f}(\mathbf{u}) + \frac{\partial \mathbf{f}(\mathbf{u})}{\partial \mathbf{u}}\Delta\mathbf{u} = \mathbf{0}\,. \tag{4.15}$$

Assuming that $\mathbf{f}(\mathbf{u})$ is a known function and that $\Delta\mathbf{u} = \mathbf{u}_{m+1} - \mathbf{u}_m$, where $\mathbf{u}_m$ is a known value of nodal displacements for the m^{th} iteration, we may solve for $\mathbf{u}_{m+1}$, the new set of nodal degrees of freedom from (4.15), as can be seen from the following, rearranged form

$$\mathbf{u}_{m+1} = -\left[\frac{\partial \mathbf{f}(\mathbf{u}_m)}{\partial \mathbf{u}}\right]^{-1} \mathbf{f}(\mathbf{u}_m) + \mathbf{u}_m . \tag{4.16}$$

Iteration is performed on Eqn. (4.16) where the function $\mathbf{f}$ is updated at each iteration taking into account material and geometric nonlinearities, until convergence is reached. Convergence is measured by ensuring that Eqn. (4.13) is satisfied to within some well-defined error tolerance. All analyses in this study have been performed using implicit time integration.

4.2 Fluid-Structure Interaction and Fluid-Fluid Interface Analyses

Two approaches have been investigated in this study for suitability in the analysis of the capillary flow problem. In the first, the Newtonian cell model is treated using a fluid (Arbitrary Lagrangian-Eulerian (ALE)) formulation and in the latter it is investigated using a solid (Lagrangian) formulation. (In the cases of the viscoelastic models a purely Lagrangian formulation for the cell has been exclusively used.) Both approaches pose particular challenges and both require the ALE formulation due to the presence of a moving fluid-fluid interface in the former case and a moving fluid-solid boundary in the latter. The ALE formulation will be presented next and its application to the two separate approaches addressed subsequently. Strictly speaking, the ALE formulation is purely mathematical and hence could have been presented in the previous section on mathematical models, however its specificity to the finite element method renders its presentation appropriate at this point in the text.

4.2.1 The Arbitrary Lagrangian-Eulerian Formulation

Introduction

In traditional solid mechanics the equations of motion are formulated expressing the independent variables (displacements and pressure if analyzing incompressible media) in material coordinates, herein referred to as $\mathbf{x}$. This is called a Lagrangian, or material, formulation. In traditional incompressible fluid mechanics the equations of motion are formulated expressing the independent variables (velocities and pressure) in spatial coordinates, herein referred to as $\mathbf{y}$. This is called an Eulerian, or spatial, formulation. In the treatment of fluid flow problems with moving boundaries (such as a free-surface, a fluid-fluid interface, or a fluid-structure interface) an intermediate formulation is used in which the equations of motion are formulated expressing the independent variables (again velocity and pressure) in what are called *mesh coordinates*, herein referred to as $\mathbf{z}$.

Preliminaries

Consider a body $\boldsymbol{B}$, fluid or solid, that in its *reference configuration*, denoted by $\boldsymbol{B_0}$, occupies the set of points in space $\mathbf{x}$. These points are then called the material

coordinates of the body. Each vector $\mathbf{x}$ (in the set of reference body points) refers to a different material particle in the body throughout the analysis, and is hence a label for each particle. At time t, the body occupies a different set of points in space, $\mathbf{y}$, and has a *current configuration* denoted $\boldsymbol{B}_t$. These points are called spatial coordinates. Each vector $\mathbf{y}$ (in the Euclidean space) refers to a different point in physical space. At any given time a material particle of the body may or may not be present at a given point $\mathbf{y}$.

We also introduce the notion of a mesh, which can be considered to be a continuum, like a body, and also has a reference configuration $\boldsymbol{M}_0$, the location of which is denoted by the mesh coordinates $\mathbf{z}$. Therefore, the same way by which the vector $\mathbf{x}$ serves as a label for the particles of the body, the vector $\mathbf{z}$ serves as a label for the mesh points of the mesh.

The following one-to-one (invertible) mappings are assumed to exist:

$$\mathbf{x} \leftrightarrow \tilde{\mathbf{y}} \tag{4.17}$$

$$\mathbf{z} \leftrightarrow \hat{\mathbf{y}} \tag{4.18}$$

where the motion of the body $\tilde{\mathbf{y}}(\mathbf{x},t)$ comes from the solution of the equations of motion, subject to the appropriate boundary and initial conditions, and the motion of the mesh $\hat{\mathbf{y}}(\mathbf{z},t)$ is an arbitrarily specified function. We differentiate $\tilde{\mathbf{y}}$ and $\hat{\mathbf{y}}$ from $\mathbf{y}$ because the former constitute *functions* which refer to the position in physical space, $\mathbf{y}$, of the labeled particles $\mathbf{x}$ and the labeled mesh points $\mathbf{z}$ for all time.

Derivatives

Partial derivatives will be taken with respect to time, holding material, spatial, and mesh coordinates fixed. It is understood that when we hold a material coordinate fixed we are following a material particle through space, when we hold a spatial coordinate fixed we are looking at a single point in physical space as material particles pass by that point, and when we hold a mesh coordinate fixed we are following a particular mesh point as it travels through space, independently of the particles that constitute the body.

The Formulation

We assume throughout this discussion that there is one frame of reference and that it is inertial. All quantities, whether measured at a moving point or not, are measured with respect to the inertial frame.

Assume the existence of a scalar field variable T, which may represent the temperature of the body. T can be written in terms of the spatial coordinates, $T(\mathbf{y},t)$, or In terms of the material coordinates, $T(\mathbf{x},t)$ since there is a one-to-one mapping from $\mathbf{x}$ to $\mathbf{y}$ and vice-versa. Because most physical laws (mass conservation, momentum conservation, energy conservation) are expressed for material particles, in general we need to take material time derivatives of functions such as T. Additionally, we wish to use a finite element mesh that can move arbitrarily in space, neither following material particles in a Lagrangian fashion, nor fixed in space in an Eulerian fashion. In order to achieve this we will need to be able to work with mesh time derivatives, since our function T and the independent variables upon which it depends are always expressed at

the mesh points **z**, which are really our nodal points in the finite element analysis, i.e. $T = T(\mathbf{z},t)$.

The total *material* time derivative of the function $T(\mathbf{y},t)$ is

$$\dot{T} \equiv \left.\frac{dT}{dt}\right|_{\mathbf{x}} = \frac{\partial T}{\partial t} + \frac{\partial T}{\partial \mathbf{y}}\left.\frac{\partial \mathbf{y}}{\partial t}\right|_{\mathbf{x}} \tag{4.19}$$

where the dependence of **y** on **x** has been used. *Eqn.* (4.19) *represents the time derivative of the function T as it is observed following the material particle* **x** *as it travels through space.* The total *mesh* time derivative of the function $T(\mathbf{y},t)$ is

$$\tilde{T} \equiv \left.\frac{dT}{dt}\right|_{\mathbf{z}} = \frac{\partial T}{\partial t} + \frac{\partial T}{\partial \mathbf{y}}\left.\frac{\partial \mathbf{y}}{\partial t}\right|_{\mathbf{z}} \tag{4.20}$$

where the dependence of **y** on **z** has been used. *Eqn.* (4.20) *represents the time derivative of the function T as it is observed following the mesh point* **z** *as it travels through space in a prescribed manner, independently of the material's motion.*

Introducing the definitions of particle of velocity, $\mathbf{v}_p$, and mesh velocity, $\mathbf{v}_m$,

$$\mathbf{v}_p \equiv \left.\frac{\partial \mathbf{y}}{\partial t}\right|_{\mathbf{x}} \tag{4.21}$$

$$\mathbf{v}_m \equiv \left.\frac{\partial \mathbf{y}}{\partial t}\right|_{\mathbf{z}} \tag{4.22}$$

and substituting Eqn. (4.20) into Eqn. (4.19) to eliminate the transient term in (4.19) we have the following expression for the material time derivative of T

$$\dot{T}(\mathbf{y},t) = \left.\frac{\partial T}{\partial t}\right|_{\mathbf{z}} + (\mathbf{v}_p - \mathbf{v}_m)\vec{\nabla}T \tag{4.23}$$

where it is noted that the velocities are measured on the moving mesh with respect to the stationary inertial frame, and the gradient operator is used to denote the spatial gradient operator $\dfrac{\partial}{\partial \mathbf{y}}$.

Interpretation

Thus the material time derivative of an arbitrary function T, which could have equally been a scalar, vector, or tensor valued function of space, **y**, and time, t, has been expressed in terms of an arbitrarily moving mesh, which is our finite element mesh. The first term in Eqn. (4.23) is the time rate of change of T following a fixed mesh point **z** (as would be measured if we were looking at a single node of a finite element mesh as it traveled through space) and the second term is the convective term, which accounts for

the time rate of change of the measured function T due to the combined effect of the moving mesh and the moving material particles. Clearly if the mesh is stationary everywhere in the domain then mesh velocity is zero and (4.23) reduces to the familiar Eulerian formulation

$$\dot{T}(\mathbf{y},t) = \frac{\partial T}{\partial t} + \mathbf{v}_m \cdot \vec{\nabla} T \,. \tag{4.24}$$

Whereas if the mesh velocity exactly coincides with the material particle velocity everywhere in the domain then (4.23) reduces to the simple Lagrangian formulation

$$\dot{T}(\mathbf{y},t) = \left.\frac{\partial T}{\partial t}\right|_{\mathbf{z}(\text{or } \mathbf{x}, \text{ they coincide})}, \tag{4.25}$$

hence the name the Arbitrary Lagrangian-Eulerian formulation.

4.2.2 Fluid-Structure Interaction: Direct vs. Iterative Approach

The following mathematical requirements must hold for all time in a fluid-structure interaction analysis to ensure that the analysis is indeed fully-coupled:

Continuity: $\mathbf{v}^{fluid} = \mathbf{v}^{solid}$ on the fluid-structure interface

Momentum: $\mathbf{t}^{fluid}_{(\mathbf{n})} = \mathbf{t}^{solid}_{(\mathbf{n})}$ on the fluid-structure interface

Where it is noted that in the case of the surface tension model, $\mathbf{t}^{solid}_{(\mathbf{n})}$ includes the stresses due to both the viscoelastic cell and its bounding surface tension.

In satisfying these conditions there are two ways to proceed. The first is termed The Iterative Approach and the second is termed The Direct Approach. It is to the discussion of these two approaches that we turn next.

The Iterative Approach proceeds as follows for a typical iteration in the analysis:

1. Given the current (computed from the previous time step or given by the initial conditions in the problem) fluid domain boundaries and boundary conditions, compute the fluid flow field.
2. Take the fluid field tractions on the fluid-structure interface from the fluid solution in (1) and impose them on the solid as natural (forcing) boundary conditions.
3. Compute the solid response subject to the given boundary conditions (from the fluid and other externally applied boundary conditions).
4. Take the displacement of the solid on the fluid-structure interface from the solid solution in (3) and impose that displacement upon the fluid domain's fluid-structure interface.

5. Loop until the increments in displacement, velocity, and force on the fluid structure-interface between the current and the previous iteration are sufficiently small (i.e. convergence has been attained).

As opposed to the direct method, in which a typical iteration looks identical to that for a purely fluid flow problem or a purely solid problem:

Solve

$$\mathbf{0} = \mathbf{R} - \mathbf{F} \tag{4.26}$$

using Newton-Raphson iteration, where $\mathbf{F}$ is the forces on the finite element nodes coming from the internal stresses in the body and includes both the fluid domain nodes, the structural domain nodes, and the nodes on the fluid-structure interface. The difficulty in this approach is that the derivatives of $\mathbf{F}$ (which result in the stiffness matrix) must be taken appropriately and a compatible time-integration scheme must be employed between the solid and fluid [19].

4.2.3 Fluid-Fluid Interface Analysis

The alternative solution approach for the Newtonian fluid with cortical tension cell model in the capillary flow problem that was investigated, developed, and found to be partially successful is that of a fluid-fluid analysis approach. That is, both the suspending fluid and the cell were treated as incompressible fluids employing the ALE formulation for both domains.

The fluid-fluid interface was treated using a Lagrangian interface-tracking scheme similar to that employed by other researchers [20]. The main difference of the scheme employed in this study was that the solution was fully implicit as opposed to explicit. The interface was tracked according to

$${}^{t+\Delta t}\mathbf{r} = {}^{t}\mathbf{r} + (\Delta t)\,{}^{t+\Delta t}\mathbf{v} \tag{4.27}$$

as opposed to an explicit scheme in which one would have

$${}^{t+\Delta t}\mathbf{r} = {}^{t}\mathbf{r} + (\Delta t)\,{}^{t}\mathbf{v}\,. \tag{4.28}$$

The implicit approach for interface tracking is consistent with the implicit approach taken in the solution of the finite element equations (see Section 4.1) and means that for each time step in the analysis, momentum, continuity, and the kinematical interface condition are met (see Section 3.1). This allows for greater solution accuracy and a significantly increased minimum time step size.

4.3 Implementation of the Neutrophil Models in ADINA

4.3.1 Newtonian Fluid Model

As can be seen from the following constitutive equation

$$\dot{\mathbf{E}}' = \frac{\mathbf{T}'}{2\mu_2} + \frac{\dot{\mathbf{T}}'}{2G_2}, \tag{4.29}$$

a Newtonian fluid is simply a Maxwell medium with an infinite elastic shear modulus ($G_2 \to \infty$). In the indentation study, the Newtonian fluid neutrophil model was implemented by assuming that the elastic shear modulus was 10,000 times larger than the average shear stresses in the model. With this assumption, the elastic strains resulting from the shear stresses were ensured to be (on average) much less than 1%. Given that the typical strains in the analyses performed in this study were very large (typically greater than 10%) this modeling assumption is appropriate. In the first capillary flow model (fluid-fluid interface formulation), however, the exact Newtonian constitutive relation was used for the Newtonian cell model.

4.3.2 Surface Tension

The surface tension model required a modification to the existing program features of ADINA. It was implemented in 2D axisymmetric analysis by assuming that an initial stress is present in the axisymmetric shell element. This initial stress was constant throughout the analysis, and hence acted like surface tension. The initial stress can be written mathematically as

$$\mathbf{F}_{\substack{\text{surface}\\\text{tension}}} = \int_{Vol} \mathbf{B}^{\mathrm{T}} \boldsymbol{\sigma}_{\text{initial}} \mathrm{dV} \tag{4.30}$$

where the volume integral extends over the beams on the surface of the cell, always in its current configuration and $\boldsymbol{\sigma}_{\text{initial}}$ is the constant stress vector corresponding to the principal directions of the shell element, in this case any two orthogonal directions tangent to the shell mid-surface.

The elastic modulus and thickness of the shell were assumed to be small (0.0001 Pa and 1 nm respectively) so that bending and other deformation-induced effects were negligible on the response.

4.4 Validation – Micropipette Aspiration

The small deformation aspiration experiment of Dong *et al.* (1988) is simulated using the Maxwell model with cortical tension (see Table III, Ref. 15) and the results are compared to Dong's simulation results using a similar (but not identical) mathematical model for the aspiration process. The original configurations of the cell and pipette geometries used in the analysis are illustrated in Figure 7 below and are identical to those in Dong *et al.*'s simulation. A step (negative) pressure of 19.6 *Pa* is applied to the portion of the cell that is interior to the pipette to simulate the step pressure drop applied by Dong *et al.* Small strains and large displacements/rotations are assumed to be consistent with Dong *et al.*'s mathematical model.

The Maxwell material properties (k_2 and η_2) and the cortical tension T_0 were chosen by Dong *et al.* to best fit the data from the aspiration experiment they were simulating. The Maxwell shear modulus of the cell is assumed to be 14.25 *Pa* with a

1.05 second decay time constant, or a viscosity of 15 *Pa s*, and the cortical tension is 31 *pN/μm*.

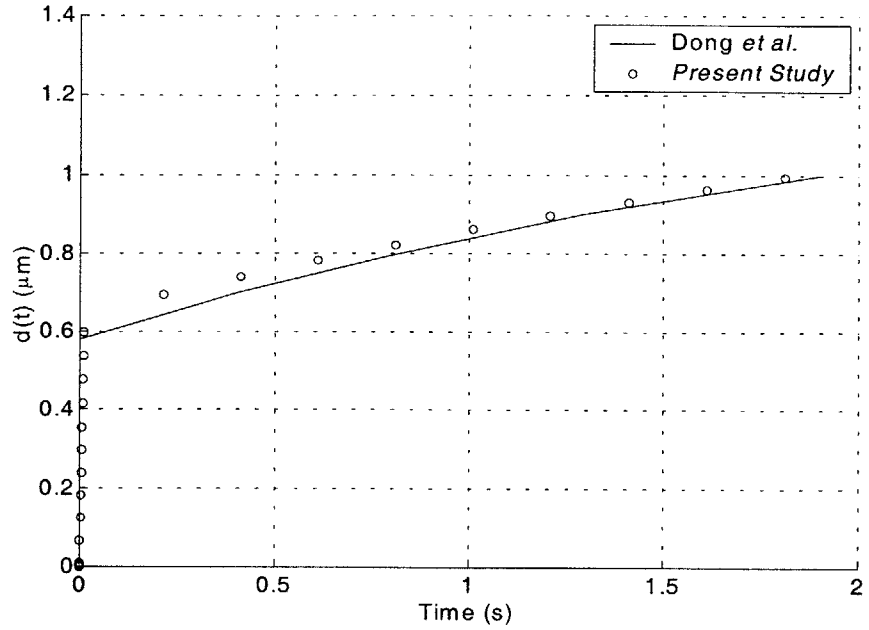

Figure 7: Maxwell model with cortical tension simulation results compared to simulation results of Dong *et al.* (1988). Model dimensions are listed in Table I and constitutive parameters in the text and Table III.

Figure 7 shows the simulation results obtained with ADINA in this study compared to the simulation results of Dong *et al.* As can be seen, agreement is good but not perfect. There are several reasons for the discrepancy between the two results. The first is that Dong *et al.* assumed the cell to be exactly incompressible, whereas in this study a Poisson's ratio of only 0.49 was assumed. The second, is that Dong *et al.* approximated the contact boundary condition and the sliding of the cell over the pipette tip as it enters by applying a ring pressure load on the cell, computing the deformation, and then translating the cell rigidly to the right by a small increment and subsequently applying another ring pressure load on the cell etc. as opposed to the analysis in this study, in which the cell's sliding across the pipette tip as it enters was explicitly accounted for using ADINA's contact algorithm. The third and last difference between the two studies is that of the finite element discretization. Dong *et al.* used eight-node 2D continuum elements for the cell's interior vs. the nine-node elements used in this study.

In Figure 7 we note the initial, instantaneous response of the cell (due to the lack of inertial and viscous effects) as it "jumps" into the pipette. This initial jump would not be captured by the Newtonian liquid droplet model, as there is no elasticity in the cell in that model.

5. Cell Indentation Results

Having validated the results from the Maxwell model used to model the cell in the physiologically relevant capillary flow simulations using the pipette experiment, next we turn to cell indentation to first show that the three published models presented in the Modeling Section do not accurately represent the response of the cell during indentation. Subsequently, the appropriate Maxwell model parameters will be determined by fitting indentation simulation data to experiment for a passive cell and two levels of FMLP-activated cells. These models will then be used in the fluid-structure interaction capillary flow simulations.

5.1 Testing the Published Models

The cell indentation experiment performed by Zahalak *et al.* [16] on passive neutrophils is simulated using each of the three models presented in Section 2 and the simulation results compared to experiment. Large strains and large displacements/rotations are assumed for all three models. These assumptions are appropriate due to the large deformations involved in the analysis, however it is noted that small strains were assumed for the pipette aspiration simulations despite the large deformations involved in those analyses to be consistent with the previous researchers' work. The pipette simulations were used for verification purposes and hence the small strain assumption was the right one, whereas here large strains are assumed to be more accurate in modeling the physics.

Results from the simulations are presented in Figure 11. The experimental result represents the downward stroke of the indenter (from Zahalak *et al.*) and corresponds to an indentation 'stiffness' of 540 pN/μm. Although this is the only quantitative result presented by Zahalak *et al.*, two additional *qualitative* features of the experimental indentation force vs. displacement curve were presented.

The first is that the indentation curve exhibits hysteresis. The force required to indent the cell during the downward stroke was significantly greater than the force required during the upward (recovery) stroke. The second observation was that the initial, indentation curve was always either linear or concave up, never concave down as predicted by the Newtonian fluid model with cortical tension (ref. Fig. 11b).
As shown by Figure 11a, the indentation force predicted by both viscoelastic models during the downward (indentation) stroke is considerably less than found experimentally. Both viscoelastic models predict a cell "stiffness" of about 130 $pN/\mu m$ (during the downward indenting stroke) versus the experimentally predicted value of 540 $pN/\mu m$. Additionally, the Maxwell model exhibits very little hysteresis, suggesting that the decay time constant associated with that model is too long, or alternatively, the viscosity is too high for the given Maxwell shear modulus.

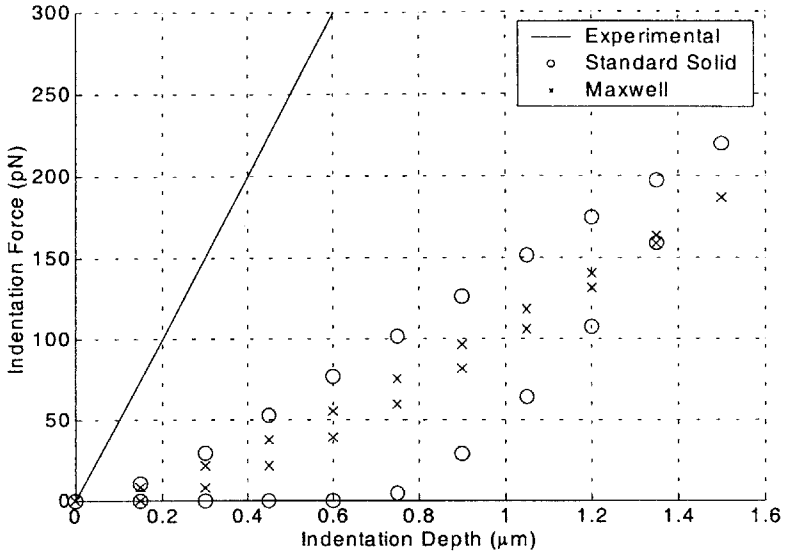

Figure 11a: Passive cell indentation results: Comparison between Maxwell model with cortical tension (G = 14.25Pa, μ = 15 Pa s, and γ = 31 pN/μm) and standard solid model (G_1 = 13.75 Pa, G_2 = 36.85 Pa, μ = 6.5 Pa s) simulation predictions and experimental results of Zahalak *et al.* (1990) for indentation force vs. depth.

In contrast with these results are those of the Newtonian model with cortical tension shown in Figure 11b. The stiffness predicted by this model is approximately 4,300 *pN/μm*, considerably larger than the experimentally determined value of 540 *pN/μm*. In addition to predicting a considerably greater cell stiffness than was found experimentally, the Newtonian model predicts that the indentation curve will be concave down during the downward (indentation) stroke of the cycle, and flat at zero force during the upward (recovery) stroke, due to the absence of elastic restoring forces in the cell. This result is consistent with the fact that the droplet has zero elasticity, and the recovery time scale for the surface tension to restore the spherical shape of the droplet is much longer than the indentation time scale of about ⅓ of a second.

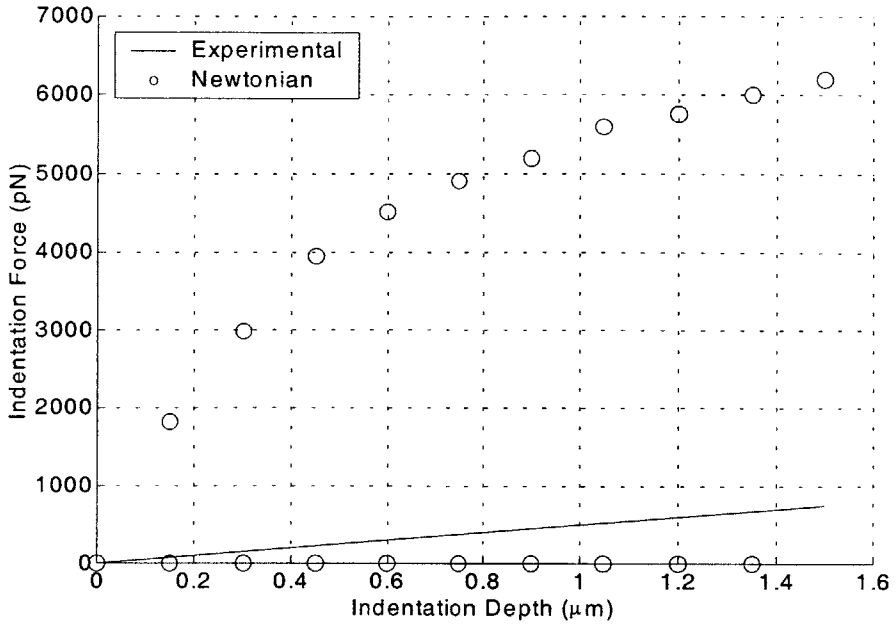

Figure 11b: Indentation results: Comparison between Newtonian model with cortical tension (μ = 105 Pa s, γ = 35pN/μm) simulation predictions and experimental results of Zahalak *et al.* (1990) for indentation force vs. depth.

5.2 Establishing New Maxwell Model Parameters for Passive and Activated Cells

Of the existing, well-established continuum neutrophil models, consisting of the homogeneous, incompressible Maxwell sphere with constant surface tension (Dong et al., 1988), the homogeneous, incompressible linear Newtonian fluid with constant surface tension (Evans and Yeung, 1989), and the homogeneous, incompressible Standard Viscoelastic Solid (Schmid-Schonbein et al., 1981), the Maxwell model was selected for use in this study. The Maxwell model incorporates the well-established surface tension-like effects of the actin-rich cortical layer lining the periphery of the cell, lying just below the external lipid bilayer, with the ability to capture both the elastic, solid-like short time-scale behavior of the cell as well as its viscous, fluid-like long time-scale behavior.

As seen by the indentation results presented in Section 5.1, however, new Maxwell model parameters are required to accurately model the cell. In this section results are presented for indentation studies that were performed exclusively with the Maxwell model with surface tension to determine appropriate values for the model parameters to model a passive, and two levels of FMLP-activated cells. Cortical tension was assumed to be independent of activation level and equal to 31 pN/μm. For this reason it was only necessary to determine the elastic shear modulus and viscosity for the different models.

Table IV summarizes the results of the parameter optimization study and Figure 12 presents the indentation results. Due to a lack of quantitative data regarding the force-displacement relation of the indenter during the upward, retracting stroke of the indenter for the activated cells, it was assumed that the time decay constant associated with the Maxwell model (μ_{cell}/G_{cell}) was constant. This was a rather ad hoc assumption that was

made due to a lack of a better alternative, and could have a significant impact on the results presented in this work.

Table IV Summary of Maxwell model parameters for various levels of FMLP-activated neutrophils. Model parameters (G, μ) were determined by systematic variation to achieve a best fit between model results and experimental indentation data.

Case #	G (Pa)	μ (Pa s)	γ (pN/μm)	Indentation Stiffness (nN/μm)	FMLP Concentration (M)
1	185	31	31	0.504	0
2	625	104	31	1.65	1e-9
3	1,350	225	31	3.48	1e-6

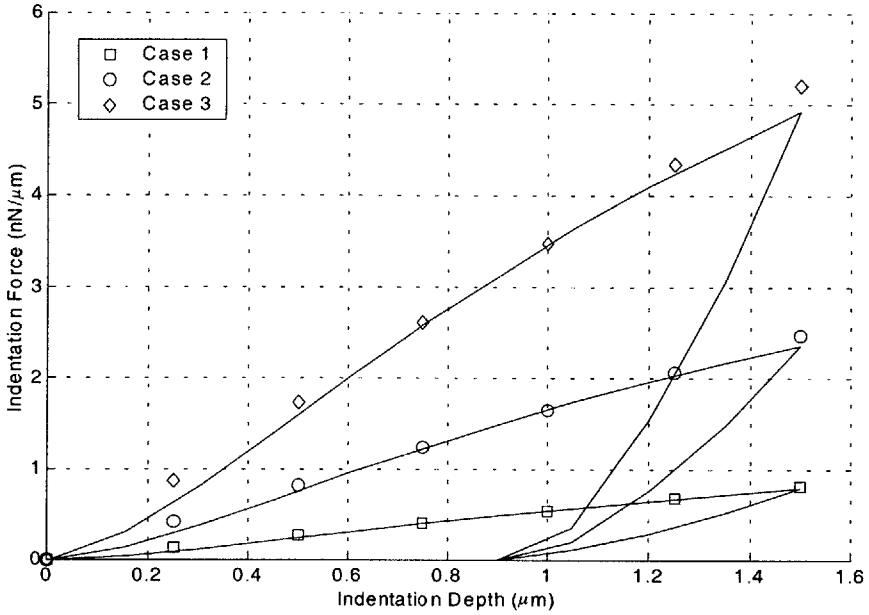

Figure 12: Maxwell model fit to experimental indentation data for a passive, 1e-9 M FMLP-activated, and 1e-6 M FMLP-activated neutrophil. Symbols represent experimental data and solid lines represent model results for Cases 1, 2, and 3 (see Table IV for best-fit Maxwell model parameters).

6. Capillary Flow Results

The capillary flow simulations were carried out with two separate models. In the first model (which essentially failed to model the physiological neutrophil-capillary flow problem of interest), the Newtonian fluid cell model with constant surface tension was simulated using the ALE formulation for both the cell and the plasma, and the Lagrangian fluid-fluid interface tracking procedure described in Section 4.2. Contact between the cell and capillary wall was not assumed, however, and therefore the cell viscosity determined by Evans and Yeung had to be drastically reduced to obtain a solution, due to the very small gap thickness present between the cell and capillary wall during its approach toward the constriction. In the second model, however, the Maxwell cell models established in Section 5.2 for passive and FMLP-activated cells are simulated using a Lagrangian formulation for the cell and the ALE formulation for the plasma. For this model contact is assumed to occur between the cell and capillary wall, and therefore the realistic cell models can be simulated, using their physiological values of viscosity and shear modulus.

6.1 Fluid-fluid Interface Model

The capillary flow simulations were carried out using the fluid-fluid interface analysis approach described in Section 4.2. Verification of the procedure was provided by simulating the axisymmetric flow of a viscous liquid droplet in a viscous suspending fluid in a rigid pipe. Analytical results for the axisymmetric flow of a *spherical* droplet due to Brenner and Hetsroni *et al.* were used for comparison. In verifying the numerical procedure, which clearly allows for deformable droplets, a low capillary number was chosen (see Appendix D) so as ensure that the droplet remained approximately spherical during the analysis and the analytical results were applicable for comparison.

Verification

Figure 13a compares the computed dimensionless average droplet velocity to the analytically predicted value for various droplet sizes and Figure 13b compares the computed dimensionless added pressure drop due to the droplet to the analytically predicted value also for various droplet sizes. Two finite element meshes, one coarse and one fine, were used to verify proper convergence of the procedure. The analytical results for these quantities are

$$\frac{U}{V} = 2 - f(\sigma)\lambda^2 + O(\lambda^3) \tag{6.1}$$

due to Hetsroni *et al.* (1970) and

$$\frac{\Delta P^+ R}{\mu_0 V} = g(\sigma)\lambda^5 + O(\lambda^{10}) \tag{6.2}$$

due to Brenner (1971), where U is the average velocity of the droplet, V is the average velocity of the suspension, σ is the ratio of the droplet viscosity to the suspending fluid viscosity, λ is the ratio of the droplet's radius to the rigid pipe's radius, μ_0 is the viscosity

of the suspending fluid, ΔP^+ is the added pressure drop due to the droplet, and $f(\sigma)$ and $g(\sigma)$ are analytically determined functions of σ (see Appendix D). Arrows in the figures denote values of λ for which the analytical results have less than 5% error.

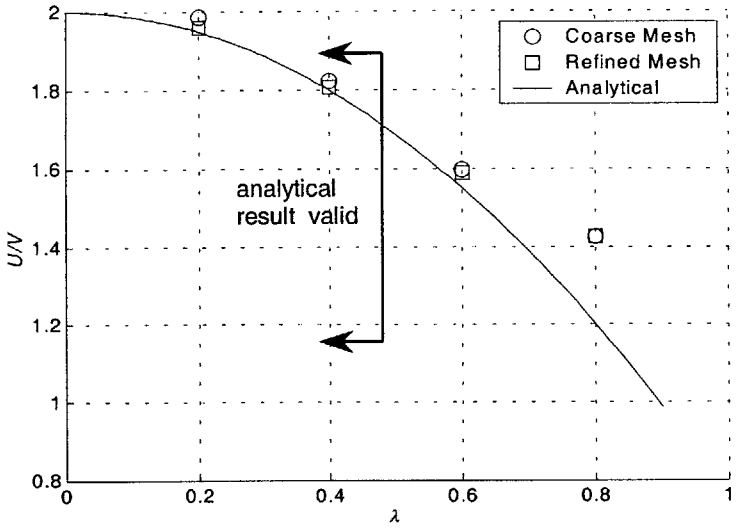

Figure 13a: Comparison of analytical and computed nondimensionalized average droplet velocity to nondimensionalized droplet size.

As the droplet becomes small ($\lambda \to 0$) the droplet velocity approaches the centerline velocity of the suspending fluid (Figure 13a). This value is twice the average velocity of the flow and the droplet is centered at the centerline of the pipe due to the axisymmetric flow assumption. As the droplet becomes small the added pressure drop due to the droplet becomes negligible (Figure 13b), as expected.

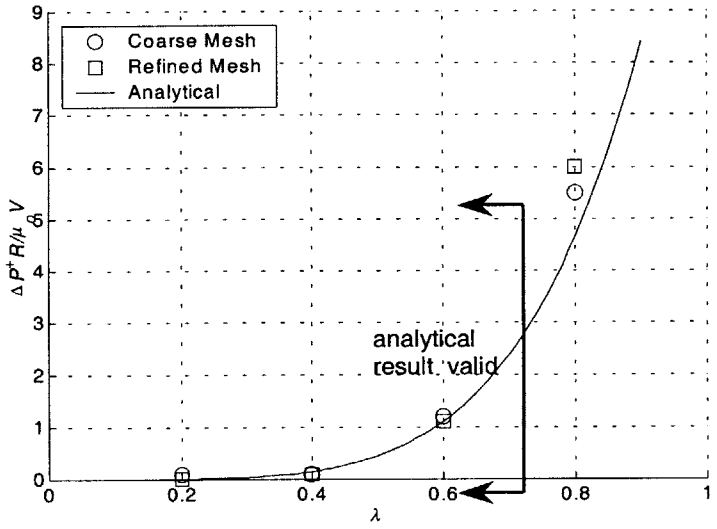

Figure 13b: Comparison of analytical and computed dimensionless added pressure drop due to the droplet vs. dimensionless droplet size.

Application to the Capillary Flow Problem

The fluid-fluid interface analysis procedure, verified above, is next applied to the simulation of a two-phase Newtonian liquid droplet with surface tension through a constriction. The constriction is a cross-sectional area reduction of 25% and is intended to represent a typical constriction found in the pulmonary microcirculation. The upstream radius of the capillary is six microns. The droplet consists of a highly viscous interior (0.1 *Pa s*) and a less viscous exterior (0.01 *Pa s*) with an outer radius of four micrometers. The interior highly viscous portion makes up 20% of the total by volume and is meant to represent the more highly viscous nucleus of a neutrophil. The surface (cortical) tension between the outer sphere and the suspending plasma is 35 $pN/\mu m$, consistent with the values obtained by Evans and Yeung. The surface tension between the inner and outer droplet fluids is 5 $pN/\mu m$ and was chosen in the absence of experimental data as a means of giving the inner fluid a restoring force. The plasma has a viscosity of that of water (0.001 *Pa s*). The density of the cell and of the plasma is that of water so buoyancy effects are absent. Furthermore, due to the very low Reynolds number of the problem, inertial effects are entirely negligible.

A constant pressure drop of 20 *Pa* is applied across the capillary segment and the solution obtained. The average velocity of the plasma is approximately 700 $\mu m/s$ as the droplet approaches the constriction. Figure 14 shows the pressure solution at a sequence of solution times and the deformation and recovery of the droplet as it passes through the constriction. At the outset of the analysis (Figure 14a), note the pressure jump between the inner and outer droplet fluids and the outer droplet fluid and the plasma due to the interfacial surface tensions. Additionally, note that the pressure gradient inside the droplet drives the inner droplet (nucleus) forward as the droplet passes through the constriction (Figures 14b and c). Finally, note the rapid recovery to sphericity of the droplet as it exits the constriction (Figures 14d and e).

It is noted that the viscosities chosen for the outer droplet fluid (0.01 *Pa s*), meant to represent the neutrophil's cytoplasm, and the inner droplet fluid (0.1 *Pa s*), meant to represent the neutrophil's nucleus, were not chosen to be the physical values determined by previous investigators (100 *Pa s* and 1000 *Pa s*, respectively). Instead, they were chosen to maintain a large enough gap between the droplet and capillary wall as it flowed through the constriction so that computational (mesh) difficulties would be avoided. This shortcoming in the analysis is discussed further in the Discussion section to follow, and does not represent a shortcoming in the numerical scheme but rather a shortcoming in the mathematical model of the neutrophil-capillary flow problem.

Due to this shortcoming, the detailed results of this capillary flow model will not be studied quantitatively, but rather we will move on to the next capillary flow model in which physiologically relevant cell model parameters are used.

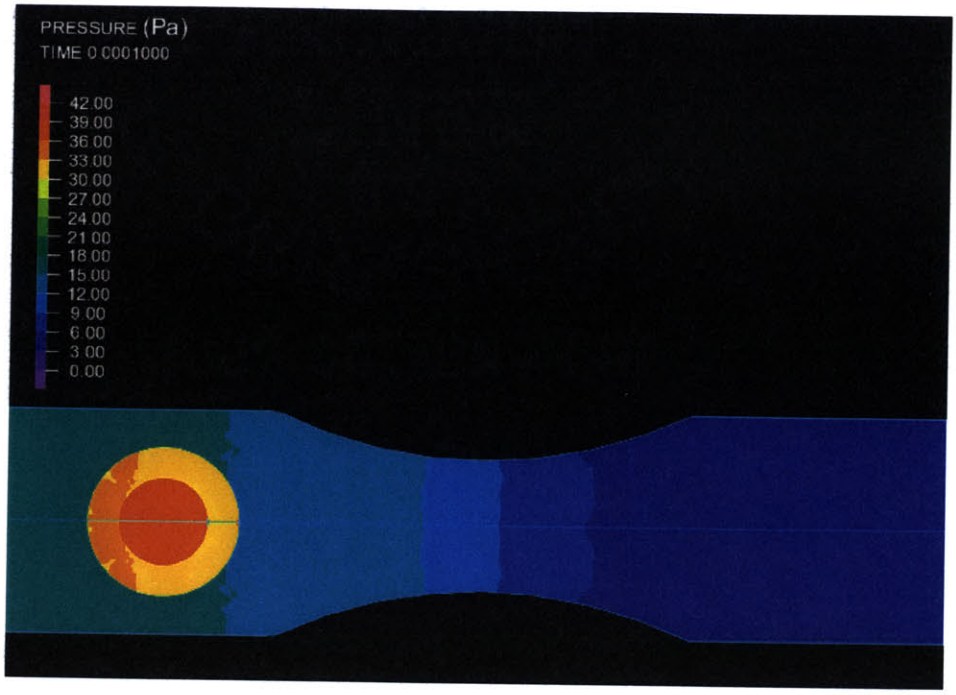

Figure 14a: Capillary flow simulation with reduced cellular viscosity (frame 1).

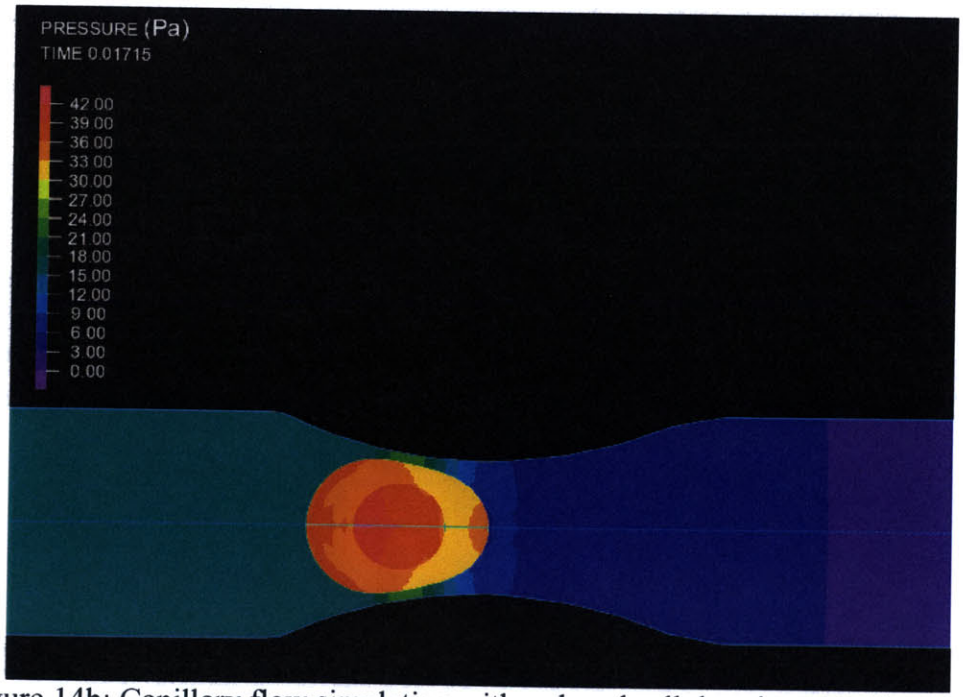

Figure 14b: Capillary flow simulation with reduced cellular viscosity (frame 2).

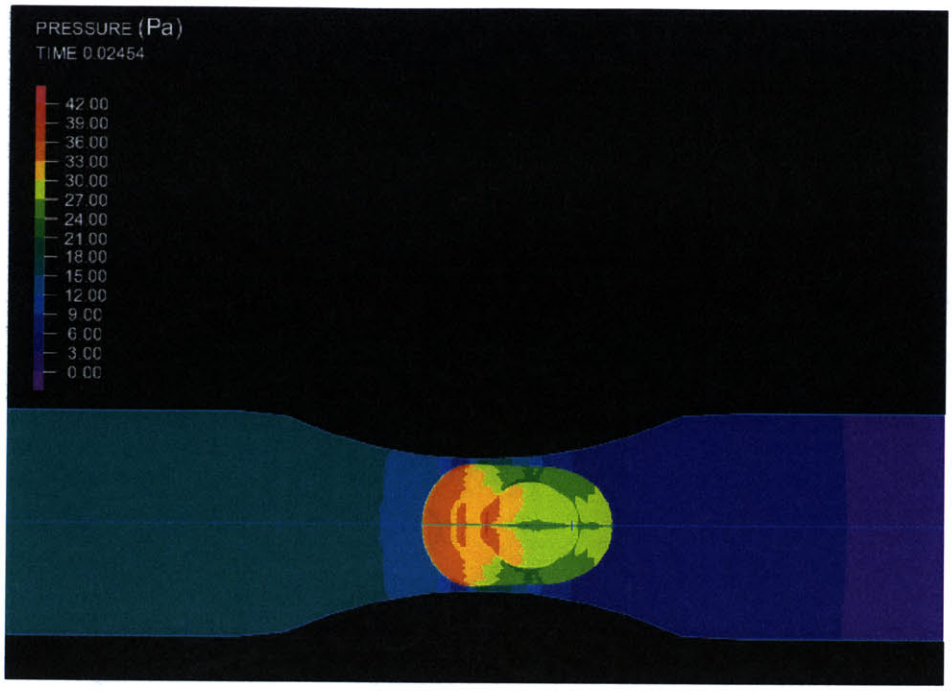

Figure 14c: Capillary flow simulation with reduced cellular viscosity (frame 3).

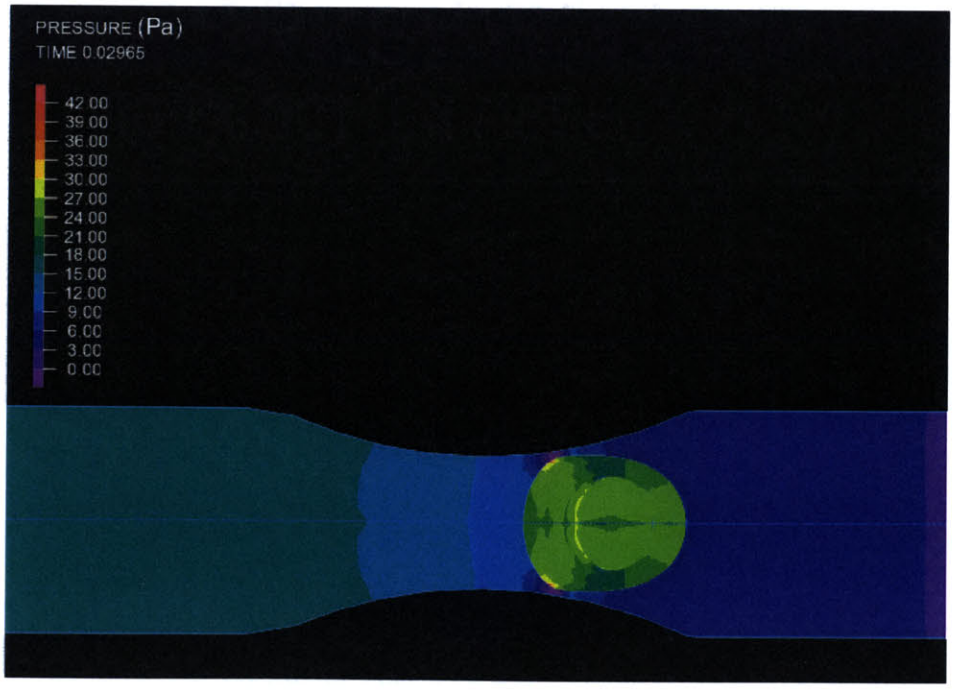

Figure 14d: Capillary flow simulation with reduced cellular viscosity (frame 4).

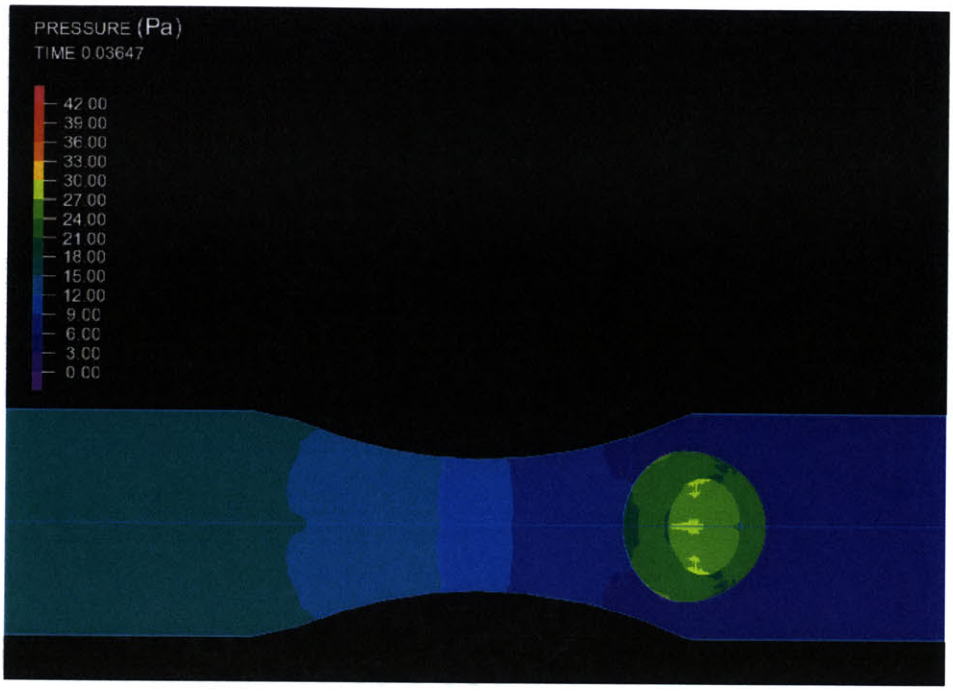

Figure 14e: Capillary flow simulation with reduced cellular viscosity (frame 5).

6.2 Fluid-structure Interaction Model

In this section results from the second (successful) neutrophil-capillary flow model are presented, in which the passive and FMLP-activated neutrophil cell models determined in Section 5.2 are employed in a fluid-structure interaction analysis assuming contact between the cell and capillary wall.

The dependence of cell transit time on minimum constriction radius, constriction radius of curvature, and cell shear modulus is investigated first. Subsequently, average cell tip velocity during capillary transit is presented for the limiting case of a large dimensionless shear modulus, and its dependence on constriction geometry is investigated.

Dimensional Analysis

The transit time, T, required for the cell to flow and deform through the capillary constriction can be expressed in its most general form as a function of all the dimensional parameters in the model

$$T = f(R_{cell}, G_{cell}, \mu_{cell}, \gamma, R_{capillary}, R_{min}, \delta, \mu_{plasma}, \Delta p, a) \tag{6.3}$$

where the transit time is defined as the time from which the leading edge of the cell crosses the capillary constriction inlet to the time when the trailing edge of the cell crosses the capillary constriction outlet. In order to reduce the number of independent dimensional parameters in Eqn. (6.3) several simplifying assumptions are made. First, it is assumed that the transit time will be nearly independent of the upstream and downstream capillary radius, $R_{capillary}$, provided that it is considerably longer than the convective time scale of the cell when it is freely traveling in the capillary ($\sim R_{cell}/\bar{V}$, where $\bar{V}$ is the average plasma velocity in the unconstricted capillary). In this limit, the bulk of the transit time consists of the time spent by the cell squeezing through the capillary constriction, during which the constant pressure drop is applied across the cell and is independent of the upstream and downstream capillary radii. Second, it is assumed that in the same limit, the capillary transit time will be insensitive to variations in plasma viscosity, μ_{plasma}, and gap thickness, δ, between the constriction contact surface and the wall. The physical reason for this is that as the cell squeezes through the constriction, there are only two retarding forces balancing the axial pressure gradient: one is due to the axial component of the normal contact traction applied to the cell by the constriction contact surface and the other is due to the Couette component of the shear stress in the gap. As shown in Appendix A, for the parameter ranges explored in this study, the retarding force due to the Couette flow induced shear stress is entirely negligible. The third and final assumption is that the effective pressure drop, Δp_{eff}, driving the cell through the constriction is given by

$$\Delta p_{eff} = \Delta p - 2\gamma\left(\frac{1}{R_{min}} - \frac{1}{R_{cell}}\right), \tag{6.4}$$

consistent with micropipette aspiration studies. This last assumption is probably the most compromising of the three, considering that in micropipette aspiration the radius of curvature of the cell interior to the pipette is very well approximated by the inner pipette radius, whereas in a gradual constriction it is somewhat questionable how well the minimum constriction radius approximates the cell's leading edge radius of curvature, which changes during flow into the constriction.

Employing the above arguments, the number of independent variables in the dimensional transit time equation above (Eqn. (6.3)) is reduced to six

$$T = g(R_{cell}, G_{cell}, \mu_{cell}, R_{min}, \Delta p_{eff}, a). \tag{6.5}$$

Choosing $\mu_{cell}/\Delta p_{eff}$ as the characteristic time scale, the dimensional transit time equation can be written in dimensionless form as

$$T^* = h\left(G^*, R^*, a^*\right) \tag{6.6}$$

where $T^* \equiv \left(T\Delta p_{eff}/\mu_{cell}\right)$, $G^* \equiv \left(G_{cell}/\Delta p_{eff}\right)$, $R^* \equiv \left(R_{min}/R_{cell}\right)$, and $a^* \equiv \left(a/R_{cell}\right)$.

The indentation results can be used with the modeling data to define physiologically relevant dimensional parameter ranges for the capillary flow simulations. They in turn can be used to define parameter ranges of interest for the three independent dimensionless variables in the model, G^*, R^*, and a^*. Using the fact that minimum constriction capillary radius ranged between 2.5 and 3 μm, constriction radius of curvature varied between about 4 and 200 μm, trans-capillary pressure drop ranged from 20 to 80 Pa, cortical tension, γ, was equal to 31 pN/μm, cellular shear modulus ranged from 185 to 1,350 Pa, and the cell's undeformed radius was assumed to be 4 μm, the following dimensionless parameter ranges of interest are determined

$$\begin{aligned} &2.47 \le G^* \le 126 \\ &0.625 \le R^* \le 0.75 \\ &1 \le a^* \le 50 \end{aligned} \tag{6.7}$$

where it is noted that the upper bound on R^* is increased to 0.85 only for the case of G^* = 100, to broaden the scope of the study. It is also important to note that the cellular viscosity, μ_{cell}, does not appear in the independent dimensionless groups because it is only used in scaling the transit time, T, to obtain the dimensionless transit time, $T^* = \left[T\left(\Delta p - \Delta p_{crit}\right)/\mu_{cell}\right]$.

Complete capillary transit results computed for the dimensionless parameter ranges indicted in Eqns. (6.7) are plotted in Figures 15a, b, and c for dimensionless minimum constriction radii of 0.625, 0.6875, and 0.75, respectively. In each figure the variation of dimensionless transit time, T^*, with dimensionless shear modulus, G^*, is shown for three different values of dimensionless constriction radius of curvature, a^*.

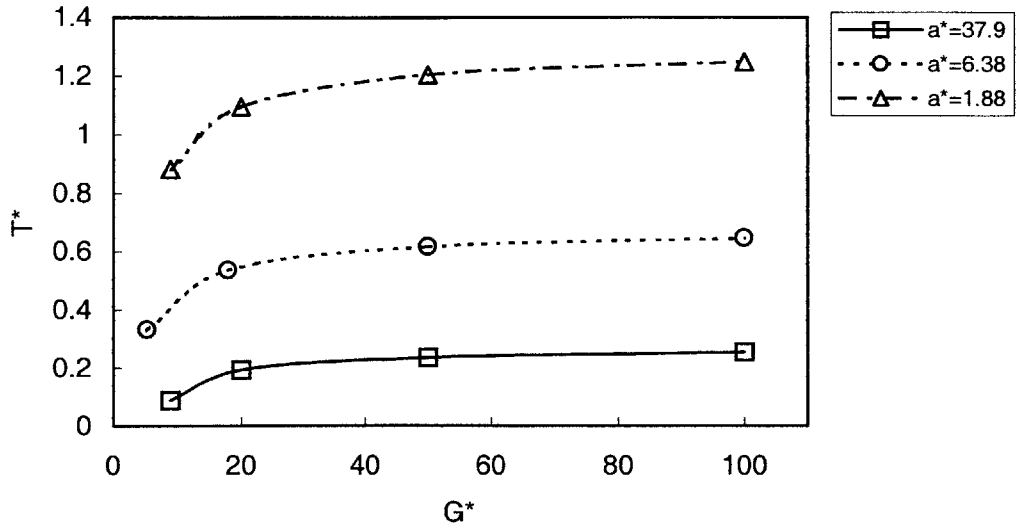

Fig. 15a Dimensionless cell transit time, $T^* \equiv \left[T\left(\Delta p - \Delta p_{crit}\right)/\mu_{cell}\right]$, vs. dimensionless cell elastic shear modulus, $G^* \equiv \left[G_{cell}/\left(\Delta p - \Delta p_{crit}\right)\right]$, for dimensionless minimum constriction radius, $R^* \equiv \left(R_{min}/R_{cell}\right) = 0.75$, and three constriction radii of curvature, $a^* \equiv \left(a/R_{cell}\right)$.

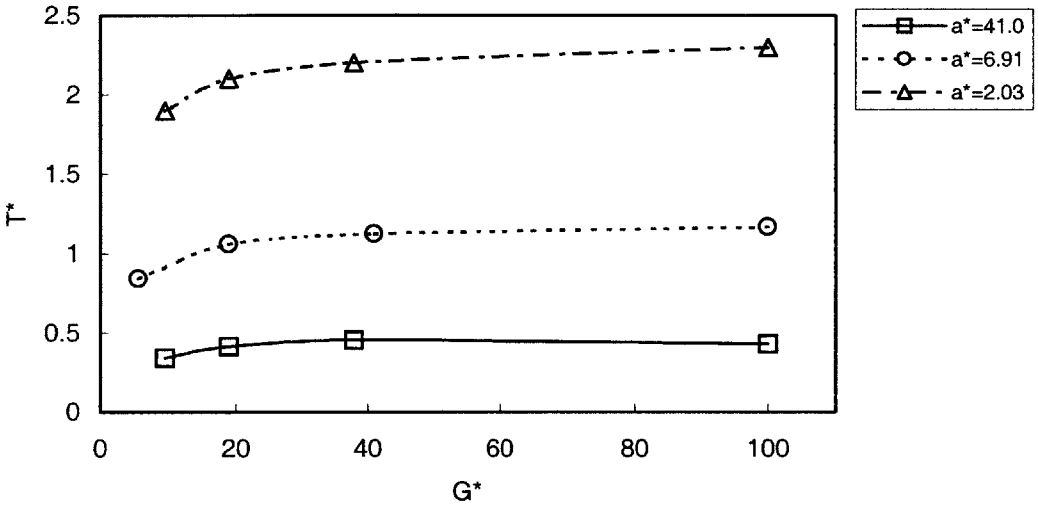

Fig. 15b Dimensionless cell transit time, $T^* \equiv \left[T\left(\Delta p - \Delta p_{crit}\right)/\mu_{cell}\right]$, vs. dimensionless cell elastic shear modulus, $G^* \equiv \left[G_{cell}/\left(\Delta p - \Delta p_{crit}\right)\right]$, for dimensionless minimum constriction radius, $R^* \equiv \left(R_{min}/R_{cell}\right) = 0.6875$, and three constriction radii of curvature, $a^* \equiv \left(a/R_{cell}\right)$.

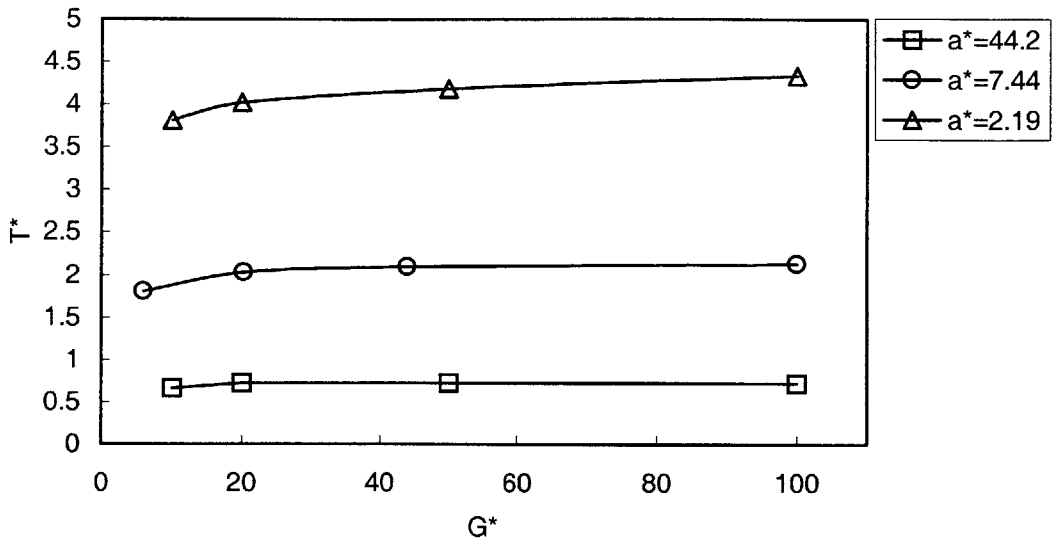

Fig. 15c Dimensionless cell transit time, $T^* \equiv \left[T\left(\Delta p - \Delta p_{crit}\right)/\mu_{cell}\right]$, vs. dimensionless cell elastic shear modulus, $G^* \equiv \left[G_{cell}/\left(\Delta p - \Delta p_{crit}\right)\right]$, for dimensionless minimum constriction radius, $R^* \equiv \left(R_{min}/R_{cell}\right) = 0.625$, and three constriction radii of curvature $a^* \equiv \left(a/R_{cell}\right)$.

For each value of dimensionless minimum constriction radius and constriction radius of curvature simulated, dimensionless transit time exhibits a clear limiting behavior as dimensionless shear modulus becomes large compared to 1, the transition occurring in each case at approximately $G^* = 20$ (Figures 15a, b, and c). The limiting behavior represents the parameter range in which the shear modulus of the cell is significantly greater than the effective driving pressure drop, so that the Maxwell model behaves essentially like a purely Newtonian fluid (i.e. elastic deformation during transit is negligible compared to total viscous deformation). For the regime $G^* < 20$, however, elastic deformation of the cell becomes significant and the reduction in transit time grows sharply as $G^* \rightarrow 1$, particularly in the mildest constriction case (ref. Fig. 15a, $R^* = 0.75$).

While dimensionless cell transit time depends strongly on minimum constriction radius, it is also exhibits a significant dependence on constriction radius of curvature for all values of minimum constriction radius analyzed. Additionally, we note that the dependence of dimensionless transit time on dimensionless constriction radius of curvature appears to be independent of G^*, the dimensionless elastic shear modulus, particularly in the viscous deformation dominated limit of $G^* > 20$. This observation is quantified in the following section, in which an empirical relationship between dimensionless transit time and dimensionless minimum constriction radius is presented for this limit.

Viscous Deformation Dominated (Newtonian) Limit

As stated in the Introduction, the primary aim of this study is to establish an empirical relationship of the form

$$T^* = g\left(G^*, R^*, a^*\right), \tag{6.8}$$

relating dimensionless neutrophil transit time to the three relevant dimensional groups in the pulmonary capillary model, representing the effects of cell elasticity and capillary geometry on neutrophil transit time.

In light of the observation that dimensionless transit time becomes independent of dimensionless shear modulus for values of $G^* >> 1$ (the transition occurring at about $G^* = 20$), we focus on this limiting (Newtonian) case, keeping the limitations of its applicability in mind, so that the dimensionless transit time relation simplifies to the following form

$$T^* = g\left(G^* >> 1, R^*, a^*\right) = h\left(R^*, a^*\right). \tag{6.9}$$

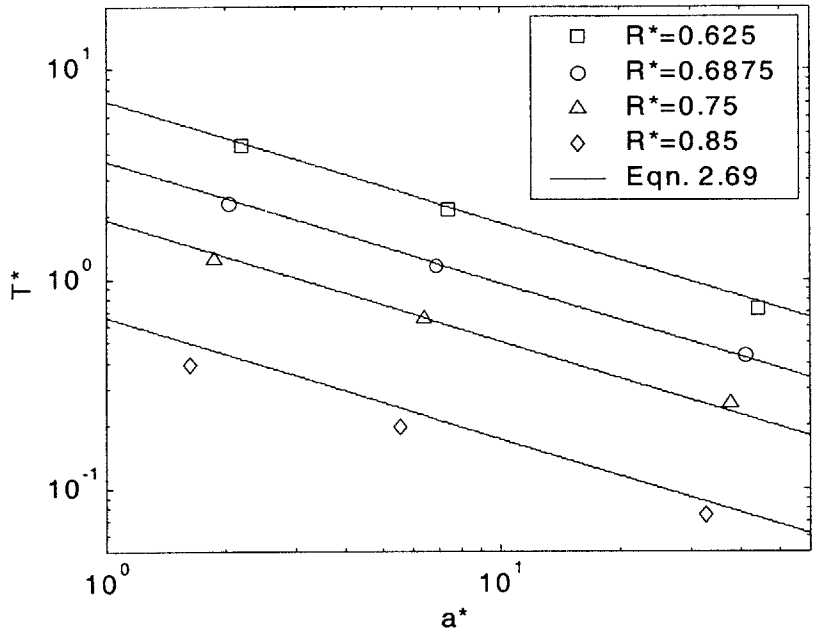

Fig. 16 Dependence of dimensionless cell transit time on dimensionless constriction radius of curvature and minimum radius for the viscous deformation dominant regime ($G^* >> 1$). Data points are from simulations and curves are given by Eqn. (6.10).

Figure 16 illustrates the computed dependence of dimensionless transit time, T^*, on dimensionless minimum constriction radius, R^*, and dimensionless constriction radius of curvature, a^*, where each simulation data point has been obtained using the value of T^* computed for $G^* = 100$ and additional data have been generated to represent the case of $R^* = 0.85$. Also plotted in Figure 16 is the following empirical relationship that was fit to the simulation data

$$T^* = 0.35\left(a^*\right)^{-0.58}\left[\left(R^*\right)^{-6.5} - 1\right]. \tag{6.10}$$

The above expression is similar in form to the simplified analytical expression presented by Yeung and Evans, (1989) for the flow of Newtonian droplets into pipettes, only in their expression there is no dependence on entrance geometry.

7. Discussion and Conclusions

Effects of Elastic Shear Modulus

Figures 15a, b, and c show that as the elastic shear modulus of a neutrophil approaches a value of about 20 times the driving trans-capillary pressure drop, the cell's transit time begins to decrease significantly. This effect is due to the fact that for a given driving pressure drop, as the cell becomes more compliant, the cell deforms elastically further and further into the constriction before getting "stuck", necessitating its viscous deformation. Thus, qualitatively speaking, as the driving pressure drop approaches the cellular shear modulus, the cell may be unhindered in its passage through the capillary constriction, particularly for mildly constricted capillaries, with minimum diameters between 6 and 8 μm. This is an effect that is not captured by the purely Newtonian cell models that assume infinite cellular shear moduli, and hence those models should be used with care when predicting neutrophil transit through mildly constricted capillaries.

Effects of FMLP on Transit Time

In looking at the effects of FMLP activation level on cell transit time, it is of interest to look at the two extremes of minimum capillary constriction radius and constriction radius of curvature analyzed in this study. In all cases it is expected that the dimensional transit will be about three times higher in the mildly activated case than in the passive case, and that the highest activation level cell will have a transit time twice that of the mildly activated cell, due to the differences in viscosity between the cells (refer to Table IV).

The dimensional pressure drop of interest is chosen to be 28 Pa, which corresponds to the low end of the pressures examined in this study, and a typical trans-capillary pressure drop found in the pulmonary microvasculature [3]. For this pressure drop and a minimum constriction radius of 2.5 μm, there are six dimensional transit times of interest. The first three correspond to a dimensionless constriction radius of curvature of about 40 and the latter three to a dimensionless constriction radius of curvature of 2. For a constriction radius of curvature of 40 and minimum constriction radius of 2.5 μm, the passive cell has a value of G^* that is equal to 10, whereas the two activated cells have values that are significantly greater than 20, at about 30 and 70, for the 1E-9M and 1E-6M cases, respectively. The transit time for the passive cell in this case was computed to be 1.1 seconds (1.5 s would be predicted using the empirical relationship (Eq. (6.10)), which is invalid for this case due to the fact that G^* is less than 20). This is in contrast to values of 5.00 and 10.8 seconds for the 1E-9 and 1E-6 M FMLP activated cells, respectively. It is interesting to note that the passive cell's low elastic shear modulus reduces its transit time by over 30% relative to the value it would have if it truly acted as a purely viscous fluid with viscosity 30.8 Pa s. In any case, however, its transit time is significantly smaller than those of the activated cells, which, are up to an order of magnitude longer in the 1E-6 M FMLP case.

When the dimensionless constriction radius of curvature is decreased to 2, for the same minimum constriction radius and pressure drop, the transit times for the passive, mildly activated, and highly activated cells are increased to 6.39, 25.0 and 54.1 s, respectively. The strong effect of not only FMLP activation level on cell transit time but also constriction radius of curvature are made clear by this example, where the passive

cell transit time increases by about a factor of 6 due to the decreased constriction radius of curvature, and the activated cell transit times increase by factors of 5 each.

For higher pressures than 28 Pa, dimensionless shear modulus for the passive case falls well below 20, and due to computational limitations this regime of parameter space could not be studied. It is worthy of note, however, that even for the FMLP-activated cells, pressures greater than about 40 Pa in the mildly activated case and greater than about 70 Pa in the highly activated case correspond to dimensionless shear moduli less than 20, and hence for these pressures the applicability of the empirical relationship determined in this study becomes questionable.

Future work would include further experimentation with neutrophils using indentation and other probing techniques. In particular, it would be of interest to have experimental indentation force-displacement data on neutrophils for various rates of indentation, so that the Maxwell constitutive parameters would better predict cellular response. For very high rates of indentation it is expected that the cell would respond purely elastically, whereas for slower rates of indentation viscous effects would be dominant. These indentation tests would test the validity of the predictive capabilities of the Maxwell models determined in this study.

In addition to further validating the accuracy of the small deformation neutrophil model used in this study, it would be of great interest to study large deformation capillary flow to determine whether the dimensionless transit time scaling relationship determined in this study holds in the large deformation regime. Even if the scaling relationship does hold, which it very well might since there are no additional effects that come into play in the model as the constriction radius is reduced, the accuracy of the relationship in terms of modeling real cells is questionable due to the lack of a nucleus in the model. If a nucleus were included in the model, the transit time relationship would acquire a different slope (T^* with respect to R^*) as the minimum constriction radius is reduced, as long as the characteristic time scale used is that of the cytoplasmic viscosity divided by the effective driving pressure.

Another issue that needs to be further studied is the effect of constriction radius of curvature on transit time. In this study the minimum radius of curvature studied was 2, corresponding to an approximate taper angle of 26°. There is a question as to whether the scaling relationship (Eqn. (6.10)) will hold as the angle approaches 90°, and further studies are required to resolve this issue (in particular as the radius of curvature goes to zero the transit time blows up in Eqn. (6.10)).

A final geometric effect that should be studied is the three dimensional effect of a non-axisymmetric constriction on cell transit time should be studied, as physiological capillaries are rarely exactly round, and this additional geometric effect is sure to have a significant effect on cell transit time.

Another significant simplification employed in this study was that of the contact surface assumption, and the neglecting of the glycocalyx, a glycoprotein rich layer bounding the inner surfaces of all capillaries (and other vessels) that might play a significant role in altering cell transit time as it possibly deforms to dynamically alter the capillary constriction diameter [21, 22].

Several lasting, novel findings have been made in this study. The first is that FMLP-activation levels strongly affect cellular elasticity and viscosity, explaining the effects on transit time through pores and pulmonary capillaries previously observed by

experimentalists such as Worthen et al. (1989). The second is that cell transit time depends on minimum constriction radius significantly more strongly (a power of –6.5 vs. –3) than found in previous micropipette models (Evans and Yeung, 1989). The third and final finding is that cell transit time is significantly affected by constriction radius of curvature, or entrance geometry, and hence capillary geometry is an important factor in considering the transit time of neutrophils through the microvasculature.

8. Acknowledgements

I gratefully acknowledge my advisor, Professor Roger D. Kamm, for his guidance, support, and extraordinary kindness and patience throughout my graduate studies.

9. Appendices

Appendix A: Cauchy Stress Tensor and Small Strain Tensor

T is defined to be the Cauchy (true) stress tensor of standard continuum mechanics texts [14]. **E** is defined to be the small strain tensor, or the symmetric part of the gradient of the displacement vector **u**,

$$\mathbf{E} = \frac{1}{2}(\vec{\nabla}\mathbf{u} + \vec{\nabla}\mathbf{u}^{\mathrm{T}}) \tag{9.1}$$

We wish to define a traceless tensor called the deviatoric stress tensor, $\mathbf{T}'$, and its counterpart the deviatoric strain tensor, $\mathbf{E}'$:

$$\begin{aligned} \mathbf{T}' &= \mathbf{T} - \frac{1}{3}T_{kk}\mathbf{I} \\ \mathbf{E}' &= \mathbf{E} - \frac{1}{3}E_{kk}\mathbf{I} \end{aligned} \tag{9.2}$$

These deviators can be shown to be traceless by simply taking the trace of both sides of each of the equations in (9.2). We can further define the mechanical pressure, p, and the volumetric strain, E_v, to be

$$\begin{aligned} p &\equiv -\frac{1}{3}T_{kk} \\ E_v &= E_{kk} \end{aligned} \tag{9.3}$$

where the volumetric strain, E_v, is equal to the trace of the strain tensor, **E**, in the limit of small strains.

Appendix B: Mechanical Energy

The mechanical energy statement

$$\int_{Vol} \rho\mathbf{b}\cdot\mathbf{v}\,dV + \int_{S}\mathbf{t}_{(\mathbf{n})}\cdot\mathbf{v}\,dS = \text{Power Input} \tag{9.4}$$

Where **v** is the velocity of a material particle at any point in the body, the volume integral accounts for the work done onto the body by externally applied body forces **b**, and the surface integral accounts for work done onto the body by externally applied tractions, $\mathbf{t}_{(\mathbf{n})}$. Substituting the definition of the traction vector, $\mathbf{t}_{(\mathbf{n})} = \mathbf{T}\mathbf{n}$, into Eqn. (9.4) we have

$$\int_{Vol} \rho \mathbf{b} \cdot \mathbf{v}\, dV + \int_{S} \mathbf{t}_{(\mathbf{n})} \cdot \mathbf{v}\, dS = \int_{Vol} \rho \mathbf{b} \cdot \mathbf{v}\, dV + \int_{S} \mathbf{T}\mathbf{n} \cdot \mathbf{v}\, dS \tag{9.5}$$

which, upon use of the transformation $\mathbf{v} \cdot \mathbf{T}\mathbf{n} = \mathbf{n} \cdot \mathbf{T}^{T}\mathbf{v}$, becomes

$$\int_{Vol} \rho \mathbf{b} \cdot \mathbf{v}\, dV + \int_{S} \mathbf{t}_{(\mathbf{n})} \cdot \mathbf{v}\, dS = \int_{Vol} \rho \mathbf{b} \cdot \mathbf{v}\, dV + \int_{S} \mathbf{n} \cdot \mathbf{T}^{T}\mathbf{v}\, dS. \tag{9.6}$$

Using the divergence theorem to transform the surface integral on the right to a volume integral we have

$$\int_{Vol} \rho \mathbf{b} \cdot \mathbf{v}\, dV + \int_{S} \mathbf{t}_{(\mathbf{n})} \cdot \mathbf{v}\, dS = \int_{Vol} \rho \mathbf{b} \cdot \mathbf{v}\, dV + \int_{Vol} \operatorname{div}(\mathbf{T}^{T}\mathbf{v})\, dV \tag{9.7}$$

which, upon expansion of the divergence term, becomes

$$\int_{Vol} \rho \mathbf{b} \cdot \mathbf{v}\, dV + \int_{S} \mathbf{t}_{(\mathbf{n})} \cdot \mathbf{v}\, dS = \int_{Vol} \rho \mathbf{b} \cdot \mathbf{v}\, dV + \int_{Vol} (\operatorname{div}\mathbf{T}^{T} \cdot \mathbf{v} + \mathbf{T} \cdot \operatorname{grad} \mathbf{v})\, dV .$$

Now if we split the gradient term on the right into its symmetric and skew-symmetric components

$$\operatorname{grad} \mathbf{v} = \frac{1}{2}(\operatorname{grad} \mathbf{v} + \operatorname{grad} \mathbf{v}^{T}) + \frac{1}{2}(\operatorname{grad} \mathbf{v} - \operatorname{grad} \mathbf{v}^{T}) \tag{9.8}$$

or using more compact notation

$$\mathbf{L} = \mathbf{D} + \mathbf{W} \tag{9.9}$$

where $\mathbf{L}$ and $\mathbf{D}$ were previously defined in Section 2.2.3 and $\mathbf{W}$ is simply the skew-symmetric part of $\mathbf{L}$, and we use the fact that the stress tensor $\mathbf{T}$ is symmetric so that

$$\mathbf{T} \cdot \mathbf{L} = \mathbf{T} \cdot (\mathbf{D} + \mathbf{W}) = \mathbf{T} \cdot \mathbf{D} \tag{9.10}$$

then we have

$$\int_{Vol} \rho \mathbf{b} \cdot \mathbf{v}\, dV + \int_{S} \mathbf{t}_{(\mathbf{n})} \cdot \mathbf{v}\, dS = \int_{Vol} (\operatorname{div}\mathbf{T}^{T} + \rho \mathbf{b}) \cdot \mathbf{v}\, dV + \int_{Vol} \mathbf{T} \cdot \mathbf{D}\, dV \tag{9.11}$$

Upon use of the momentum theorem we have the final form

$$\int_{Vol} \rho \mathbf{b} \cdot \mathbf{v}\, dV + \int_{S} \mathbf{t}_{(\mathbf{n})} \cdot \mathbf{v}\, dS = \int_{Vol} \rho \dot{\mathbf{v}} \cdot \mathbf{v}\, dV + \int_{Vol} \mathbf{T} \cdot \mathbf{D}\, dV \tag{9.12}$$

which states that the rate of working on a body by external body forces and tractions goes into increasing the kinetic energy of the body and internal working on the body (either elastic energy storage by the body or dissipation in the body).

In deriving The Principle of Virtual Work we simply replace the velocity vector, **v**, that was used as a starting point in the above derivation with the virtual displacement vector, $\delta\mathbf{u}$, and proceed in the same manner. It is interesting to note that the fact that the body is made of an elastic, viscous, or viscoelastic material does not enter into Eqn. (9.12) or the theorem until we actually consider the precise constitutive law of the material. Eqn. (9.12) is simply an instantaneous energy balance and must hold regardless of the material.

Appendix C: Gap Thickness

Using order of magnitude scaling analysis, the axial pressure force exerted on the cell during transit can be approximated as

$$F_p \sim (\Delta p - \Delta p_{crit}) R^2 \tag{9.13}$$

where Δp is the constant trans-capillary pressure drop, Δp_{crit} has been previously defined, and R is either the initial cell radius or the minimum constriction radius, they are indistinguishable for an order of magnitude analysis. The axial retardation force exerted on the cell by fluid shear stress can be approximated as

$$F_\tau \sim \tau R^2 \tag{9.14}$$

where τ can be approximated as the Couette component of the flow field in the gap as

$$\tau \sim \mu_{plasma} \frac{R/T}{\delta} \tag{9.15}$$

where the velocity gradient in the gap has been approximated as the cell radius, R, divided by the transit time, T, times the constant gap thickness, δ.

For the transit time to be independent of the gap thickness and plasma viscosity, it must hold that

$$F_p \gg F_\tau \tag{9.16}$$

or

$$(\Delta p - \Delta p_{crit}) R^2 \gg \mu_{plasma} \frac{R}{T\delta} R^2 \tag{9.17}$$

which can be written in dimensionless form as

$$T^* \gg \frac{\mu^*}{\delta^*} \tag{9.18}$$

where

$$T^* = \frac{T(\Delta p - \Delta p_{crit})}{\mu_{cell}}$$

$$\mu^* = \frac{\mu_{plasma}}{\mu_{cell}} \tag{9.19}$$

$$\delta^* = \frac{\delta}{R_{cell}}$$

Since we are interested in obtaining the maximum lower bound to T^* in Eqn. (9.18), we can use the minimum cell viscosity utilized in the study to obtain

$$T^* \gg 1.3E-3\,. \tag{9.20}$$

Thus, as long as the dimensionless transit times in this study are orders of magnitude greater than 1.3E-3, the effect of gap shear stress on cell transit will be negligible.

From Eqn. (9.20), we can also determine what the necessary gap thickness would be in order to have an effect on the transit time results. For dimensionless transit times of order 1, gap shear stress would significantly affect cell transit time when

$$\mu^* \sim \delta^* \tag{9.21}$$

or, using again the maximum value of μ*, we have that the critical gap thickness would be about 0.13 nm.

10. References

[1] http://www.britannica.com/bcom/eb/article/4/0,5716,108654+23+106084,00.html, 1999-2000, Britannica.com.

[2] Downey, GP. Invited Editorial on "Effect of mechanical deformation on structure and function of polymorphonuclear leukocytes." *Journal of Applied Physiology* **82**: 1395-1396, 1997.

[3] Huang, Y, Doerschuk, C, and Kamm, RD. Compuatational modeling of RBC and neutrophil transit through the pulmonary capillaries. *Journal of Applied Physiology* **90**: 545-564, 2001.

[4] Evans, E, and Kukan, B. Passive Material Behavior of Granulocytes Based on Large Deformation and Recovery After Deformation Tests. *Blood* **64**: 1028-1035, 1984.

[5] Schmid-Schönbein, GW, Sung, K-LP, Tözeren, H, Skalak, R, and Chien, S. Passive Mechanical Properties of Human Leukocytes. *Biophysical Journal* **36**: 243-256, 1981.

[6] Dong, C, and Skalak, R. Leukocyte Deformability: Finite Element Modeling of Large Viscoelastic Deformation. *Journal of Theoretical Biology* **158**: 173-193, 1992.

[7] Drury, JL, and Dembo, M. Hydrodynamics of Micropipette Aspiration. *Biophysical Journal* **76:** 110-128, 1999.

[8] Yeung, A, and Evans, E. Cortical shell-liquid core model for passive flow of liquid-like spherical cells into micropipets. *Biophysical Journal* **56**: 139-149, 1989.

[9] Schmid-Schönbein, G.W., Shih, Y.Y., and Chien, S., "Morphometry of Human Leukocytes," *Blood*, Vol. 56, No. 5, 1980, pp. 866-875.

[10] Tran-Son-Tay, R, Kan, HC, Udaykumar, HS, Damay, E, Shyy, W. Rheological modeling of leukocytes. *Medical & Biological Engineering & Computing* **36**, 246-250, 1998.

[11] Kan, HC, Shyy, W, Udaykumar, HS, Vigneron, P, and Tran-Son-Tay, R. Effects of Nucleus on Leukocyte Recovery. *Annals of Biomedical Engineering* **27**: 648-655, 1999.

[12] Evans, E, and Yeung, A. Apparent viscosity and cortical tension of blood granulocytes determined by micropipet aspiration. *Biophysical Journal* **56**: 151-160, 1989.

[13] Zhelev, DV, Needham, D, and Hochmuth, RM. Role of the Membrane Cortex in Neutrophil Deformation in Small Pipets. *Biophysical Journal* **67**: 696-705, 1994.

[14] Malvern, LE. *Introduction to the Mechanics of a Continuous Medium*, Prentice-Hall: New Jersey, 1969.

[15] Dong, C, Skalak, R, Sung, K-LP, Schmid-Schönbein, GW, and Chien, S. Passive Deformation Analysis of Human Leukocytes. *Journal of Biomechanical Engineering* **110**: 190-199, 1988.

[16] Zahalak, GI, McConnaughey, WB, and Elson, EL. Determination of Cellular Mechanical Properties by Cell Poking, With an Application to Leukocytes. *Journal of Biomechanical Engineering* **112**: 283-294, 1990.

[17] Bathe, K.J., *Finite Element Procedures*, Prentice-Hall, New Jersey, 1996.

[18] ADINA System User Manuals, 2001, ADINA *Theory and Modeling Guides*, ADINA R&D, Inc.

[19] Rugonyi, S, and Bathe, KJ. On finite element analysis of fluid flows fully coupled with structural interactions. *Computer Modeling in Engineering and Science* **2:** 79-96, 2001.

[20] Kan, H-C, Udaykumar, HS, Shyy, W, and Tran-Son-Tay, R. Hydrodynamics of a compound drop with application to leukocyte modeling. *Physics of Fluids* **10** (4): 760-774, 1998.

[21] Feng, J, and Weinbaum, S. Lubrication theory in highly compressible porous media: the mechanics of skiing, from red cells to humans. *Journal of Fluid Mechanics* **422**: 281-317, 2000.

[22] Pries, AR, Secomb, TW, and Gaehtgens, P. The endothelial surface layer. *European Journal of Physiology* **440**: 653-666, 2000.